

Bow shocks, bow waves, and dust waves. IV. Shell shape statistics

William J. Henney,[★] Jorge A. Tarango-Yong, Luis Ángel Gutiérrez-Soto,[†] & S. J. Arthur

Instituto de Radioastronomía y Astrofísica, Universidad Nacional Autónoma de México, Apartado Postal 3-72, 58090 Morelia, Michoacán, México

Accepted XXX. Received YYY; in original form ZZZ

ABSTRACT

Stellar bow shocks result from relative motions between stars and their environment. The interaction of the stellar wind and radiation with gas and dust in the interstellar medium produces curved arcs of emission at optical, infrared, and radio wavelengths. We recently proposed a new two-dimensional classification scheme for the shape of such bow shocks, which we here apply to three very different observational datasets: mid-infrared arcs around hot OB stars; far-infrared arcs around luminous cool stars; and H α emission-line arcs around proplyds and other young stars in the Orion Nebula. For OB stars, the average shape is consistent with simple thin-shell models for the interaction of a spherical wind with a parallel stream, but the diversity of observed shapes is many times larger than such models predict. We propose that this may be caused by time-dependent oscillations in the bow shocks, due to either instabilities or wind variability. Cool star bow shocks have markedly more closed wings than hot star bow shocks, which may be due to the dust emission arising in the shocked stellar wind instead of the shocked interstellar medium. The Orion Nebula arcs, on the other hand, have both significantly more open wings and significantly flatter apexes than the hot star bow shocks. We test several possible explanations for this difference (divergent ambient stream, low Mach number, observational biases, and influence of collimated jets), but the evidence for each is inconclusive.

Key words: circumstellar matter – methods: statistical – stars: winds, outflows

1 INTRODUCTION

Stellar bow shocks are produced by the relative motion between a star and its surrounding medium, and are commonly detected as curved arcs of emission at optical (Gull & Sofia 1979; Brown & Bomans 2005), infrared (van Buren & McCray 1988; Kobulnicky et al. 2016), or radio (van Buren et al. 1990; Benaglia et al. 2010) wavelengths. The canonical theory for these objects is that they are formed by a two-shock interaction between the stellar wind and the interstellar medium (Pikel’ner 1968; Dyson & de Vries 1972), which is distorted due to the supersonic motion of the star (Baranov et al. 1970; Wilkin 1996). In some instances, however, the absorbed stellar radiation pressure may be more important than the stellar wind in providing the inner support for the bow shell (Henney & Arthur 2019a, Paper I) and this may even be sufficient to break the collisional coupling between gas and dust grains (Henney & Arthur 2019b, Paper II). We have proposed a diagnostic method to distinguish between these cases, based on the bow shock size and the luminosity ratio between the bow shock and the star (Henney & Arthur 2019c, Paper III). In other cases, the appearance of an infrared emission arc may be due to the illumination of the inner wall of an asymmetrical cavity (Mackey et al. 2016), rather than the

formation of a dense shell, in which case the relative velocity of the star may be subsonic with respect to its surroundings (Mackey et al. 2015).

The largest number of bow shocks have been detected around high-mass OB stars, via their mid-infrared dust emission (van Buren et al. 1995; Noriega-Crespo et al. 1997; Povich et al. 2008; Kobulnicky et al. 2010; Peri et al. 2012, 2015; Sexton et al. 2015; Kobulnicky et al. 2016; Bodensteiner et al. 2018), and these have typical sizes ranging from 0.01 pc to 1 pc. In particularly dense environments, such as the inner Orion Nebula (Smith et al. 2005) and the Galactic center region (Geballe et al. 2004) they may be as small as 0.003 pc and emit at near-infrared wavelengths (Tanner et al. 2005; Sanchez-Bermudez et al. 2014). Cometary ultracompact H II regions detected at radio wavelengths (Reid & Ho 1985; Wood & Churchwell 1989; Klaassen et al. 2018) have also been interpreted as bow shocks (van Buren et al. 1990; Mac Low et al. 1991), although alternative models, such as a champagne flow caused by steep density gradients (Cyganowski et al. 2003; Arthur & Hoare 2006; Immer et al. 2014; Steggle et al. 2017), are favored in many cases. This illustrates a broader point: that it can be difficult to identify bow shocks from morphology alone, since other processes can give rise to emission arcs. In particular, curved ionization fronts, as seen in evaporating globules (Sahai et al. 2012) and proplyds (O’Dell et al. 1993) can be mistaken for bow shocks. Kinematic observations can potentially resolve such ambiguities but are not always available.

Stellar bow shocks are also observed around other types of

[★] Email: w.henney@irya.unam.mx

[†] Current address: Observatório do Valongo, Universidade Federal do Rio de Janeiro, Ladeira Pedro Antonio 43, 20080-090 Rio de Janeiro, Brazil

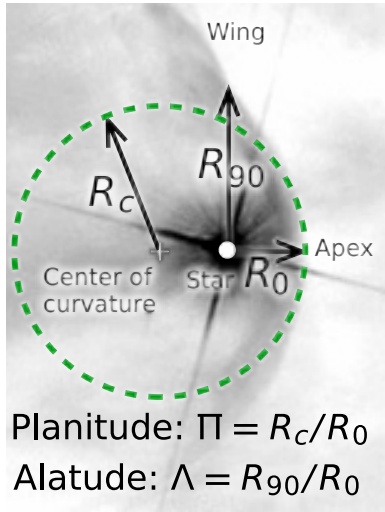


Figure 1. Terminology employed in this paper to describe bow shock shapes, following Tarango-Yong & Henney (2018, Paper 0).

stars. Bow shocks around cool red supergiant and asymptotic giant branch stars are detected at mid-infrared and far-infrared wavelengths (Ueta et al. 2006, 2008; Sahai & Chronopoulos 2010; Cox et al. 2012). Pulsar bow shock nebulae are detected principally by their $H\alpha$ emission (Kulkarni & Hester 1988; Brownsberger & Romani 2014). In the Orion Nebula (M42, NGC 1976), at least three different classes of stellar bow shock have been identified. As well as a small number of OB bow shocks (Smith et al. 2005; O’Dell 2001), bow shocks are also seen around the closest proplyds to the dominant O star θ^1 Ori C (Hayward et al. 1994; Bally et al. 1998; Robberto et al. 2005). The proplyds (O’Dell et al. 2008) are photoevaporating protoplanetary disks around low-mass young stars (Johnstone et al. 1998) and the bow shocks have been modeled as the interaction between the disk’s ionized photoevaporation flow and the supersonic stellar wind from θ^1 Ori C (García-Arredondo et al. 2001). The third class of Orion Nebula bow shock is the LL Ori-type objects (Gull & Sofia 1979; § 5 of Bally et al. 2000; § 3.2 of Bally & Reipurth 2001; Henney et al. 2013), which tend to be found in the outer regions of the nebula. These are probably due to interactions between the Orion Nebula’s champagne flow (Zuckerman 1973) and outflows from T Tauri stars, which may or may not be proplyds (Bally et al. 2000; Gutiérrez-Soto 2015).

The shapes of stellar bow shocks are frequently compared with what has become known as the *wilkinoid* surface (Cox et al. 2012), which is the result of the idealized interaction between a spherical wind and a plane-parallel stream in the hydrodynamic thin-shell approximation. Numerical approximations to this shape were used by various authors (Baranov et al. 1971; Mac Low et al. 1991) before an elegant analytic solution was found by Wilkin (1996) and extended to the case of interaction between two spherical winds (Canto et al. 1996). In Tarango-Yong & Henney (2018, hereafter, Paper 0) the study of bow shock shapes and their projection on the plane of the sky was formalized. The term *cantoid* was introduced for the Canto et al. (1996) family of shapes, together with *ancantoid* for a generalization to the case where one of the winds is anisotropic, as is appropriate for the proplyds. In addition, Paper 0 proposed the use of two dimensionless parameters, *planitude* and *alatude*, to describe a general bow shock shape, which we illustrate in Figure 1. The planitude, $\Pi = R_c/R_0$, measures the flatness of the bow shock apex, where R_0 is the star–apex distance and R_c is the radius of

curvature measured at the apex. The alatude, $\Lambda = R_{90}/R_0$, measures the openness of the bow shock wings, where R_{90} is the lateral size of the bow, measured from the star in the direction perpendicular to the star–apex direction.

In this paper, we investigate the shapes of stellar bow shocks by calculating the distributions of planitude and alatude for different classes of bow shock source. The remainder of the paper is organized as follows. In § 2 we present an analysis of the shapes of several hundred bow shock candidates associated with OB stars from the 24 μ m survey of Kobulnicky et al. (2016). Our algorithm for automatically fitting and tracing the shapes is described in § 2.1, together with our “star rating” system for evaluating the fit quality, while in § 2.2 we locate the sources on the planitude–alatude plane. In § 2.3 we study the correlations amongst non-shape parameters of the bow shock sources, such as angular size and stellar magnitude, while in § 2.4 we explore the correlations between these parameters and the planitude and alatude. In § 3 we compare with results for bow shocks around cool luminous stars and in § 4 we compare with results for stationary emission-line arcs in the Orion Nebula. In § 5 we discuss the implications of our findings for physical models of bow shock formation in the different classes of sources, and in § 6 we summarise our results. Further details of the statistical tests that we have applied are provided in Appendix A and a simple model for time-dependent oscillations of the bow shock surface is presented in Appendix B.

2 MID-INFRARED ARCS AROUND EARLY-TYPE STARS

The most extensive observational sample of stellar bow shock nebulae to date is a catalog of 709 arcs (Kobulnicky et al. 2016) detected in mid-infrared surveys of the Galactic Plane by the *Spitzer Space Telescope* (SST, Werner et al. 2004) and *Wide-field Infrared Survey Explorer* (WISE, Wright et al. 2010). These sources are believed to be powered by the winds of early-type stars, which are either moving supersonically through the interstellar medium (runaway stars, Gvaramadze & Bomans 2008), or are interacting with a local bulk flow, such as the champagne flow from a nearby H II region (weather vanes, Povich et al. 2008).

2.1 Automatic tracing and fitting of bow shocks

In order to study the shapes of these bow shocks, we downloaded data from the NASA/IPAC Infrared Science Archive archive¹ and extracted 4’ square images in the 24 μ m bandpass of the Multiband Imaging Photometer for *Spitzer* (MIPS) centered on each of the 471 Kobulnicky et al. (2016) sources that are covered by the MIPS GAL (Carey et al. 2009) survey, which includes most of the sources with Galactic longitude within $\pm 60^\circ$ of the Galactic center.

We have developed a method for automatically tracing the arcs and determining their planitude and alatude, which is an extension of the method described in Appendix E of Paper 0. The steps of the method are as follows:

1. Calculate arrays of celestial coordinates, C , for each pixel of the image. In our implementation of the method we use functions from the Python library `astropy.coordinates` (Astropy Collaboration et al. 2018).

¹ http://irsa.ipac.caltech.edu/docs/program_interface/api_images.html

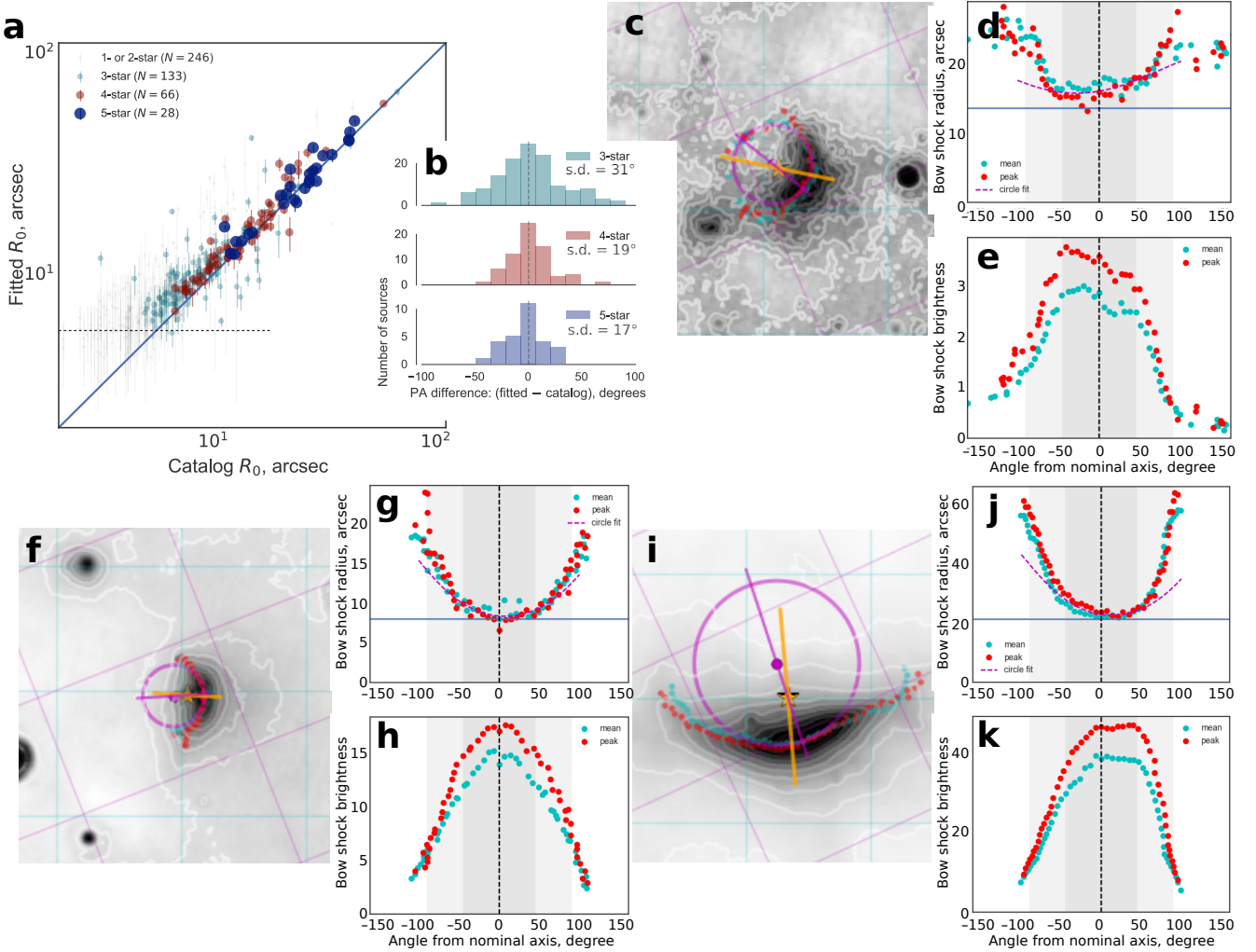


Figure 2. Examples of typical fits to the bow shock shapes of MIPS GAL sources. (a) Scatter plot of the bow shock sizes determined from our fits, as compared with those tabulated by Kobulnicky et al. (2016, K16) for the MIPS GAL sources. Different symbol sizes and colors correspond to different star ratings, which indicate our subjective judgement of the quality of the fit. The horizontal dotted line shows the MIPS $24\mu\text{m}$ point spread function FWHM of $5.5''$. (b) Histograms of the difference in bow shock position angles between our fits and the K16 values for sources with 3- to 5-star ratings. (c–e) Source K510, with a 3-star rating. (f–h) Source K506, with a 4-star rating. (i–k) Source K517, with a 5-star rating. Panels (c, f, i) show a $24\mu\text{m}$ gray-scale image of a $160'' \times 160''$ field of view, centered on each source. Contours are ten linearly spaced levels between the median brightness of the entire image and the maximum brightness of the bow shock arc. Grids of galactic coordinates (light blue lines, parallel to the box sides) and equatorial coordinates (tilted magenta lines) are shown. The stellar source and the bow shock axis, as determined by Kobulnicky et al. (2016) are indicated by an orange star and an orange line, respectively, where the line extends from $-2R_0$ to $+2R_0$. The automatically traced arc shapes using the “mean” and “peak” methods (see text) are shown by blue and red dots, respectively. The magenta circle shows the fit to the arc points within $\pm 45^\circ$ of the nominal bowshock axis, with the magenta dot showing the center of curvature and the magenta line showing the fitted bow shock axis, which is the line passing through the source and the center of curvature. Panels (d, g, j) show plots of the radius measured from the source of the arc points, plotted as a function of angle θ from the nominal bow shock axis, and with the same color coding as used on the image. Angular ranges of $\theta = \pm 45^\circ$ and $\pm 90^\circ$ are shown by gray shaded boxes. The R_0 value tabulated by Kobulnicky et al. (2016) is shown by a horizontal blue line. Panels (e, h, k) show equivalent plots for the surface brightness.

2. Using the central source coordinates, C_0 and nominal bowshock radius, R_0 from Kobulnicky et al. (2016), construct a pixel mask that includes only those pixels with separations from the source that satisfy $\frac{1}{2}R_0 \leq |C - C_0| \leq 3R_0$. This mask will be used for all subsequent operations, which serves to help avoid confusion from the star itself and other bright sources in the field of view.
3. Define a “step-back” point, C_1 , which is located at a separation $2R_0$ from the source, but in the opposite direction from the apex of the bow shock. That is, along a position angle 180° from the

nominal position angle, PA_0 , of the bow shock axis. This point is at one end of the orange line shown superimposed on the bow shock images in Figure 2.

4. Looping over a grid of 50 position angles, PA_k , within $\pm 60^\circ$ of PA_0 , estimate the location of the arc along rays cast from the step-back point, using two different methods:

- (a) The pixel with the peak brightness, with coordinates $C_{k,\text{peak}}$ (red dots in Fig. 2).

- (b) The mean brightness-weighted separation from C_1 , with coordinates $C_{k,\text{mean}}$ (light blue dots in Fig. 2).

For each PA_k in the grid, the calculation is performed over only those pixels that satisfy $|PA(C, C_1) - PA_k| < \frac{1}{2}\delta\theta$, where $\delta\theta = 120/50 = 2.4^\circ$, which defines a thin radial wedge from C_1 . The results are shown as red and blue dots superimposed on the images in Figure 2. Each of the two methods, “peak” and “mean”, works better in some objects and worse in others (according to the subjective judgment of “correctly” tracing the bow shock shape). We therefore take the average by amalgamating all the $C_{k,\text{peak}}$ and $C_{k,\text{mean}}$ points into a single set, C_k , for the following steps. We have found that the use of the step-back point greatly improves the reliability of the method, as compared with the simpler option of tracing rays from the stellar source.

5. For each of the points C_k , determine the radial separation from the central source, $R_k = |C_k - C_0|$ and the angle from the bow shock axis about the central source $\theta_k = PA(C_k, C_0) - PA_0$. These are plotted in the upper left panels of Figure 2. Note that, even though the rays are cast from the step-back point C_1 within $\pm 60^\circ$ of PA_0 , the angles θ_k are measured from the source, C_0 , which is closer to the bow shock than C_1 and therefore $|\theta_k|$ can be much larger than 60° .
6. Make our own estimate of the axial size, R_0 , of the bow shock by calculating the mean of R_k over all points C_k with $|\theta_k| \leq 10^\circ$. Note that this is distinct from the nominal value of R_0 given in the Kobulnicky et al. (2016) catalog, which was “measured by eye”. We denote by $\epsilon(R_0)$ the standard deviation of the R_k that go into calculating R_0 .
7. Estimate the radius of curvature, R_c , by fitting a circle to all those points within $\pm 45^\circ$ of the nominal axis ($|\theta_k| < 45^\circ$), but after excluding any point with $R_k < \frac{1}{2}R_m$ or $R_k > 2R_m$, where R_m is the median R_k for $|\theta_k| < 45^\circ$.
8. Determine two separate estimates, R_{90+} and R_{90-} , of the perpendicular radius, R_{90} , by taking the mean of R_k over all points C_k with $|\theta_k - 90^\circ| \leq 10^\circ$ for R_{90+} , and with $|\theta_k + 90^\circ| \leq 10^\circ$ for R_{90-} . The average of the two standard deviations of the R_k that contribute to R_{90+} and R_{90-} is denoted by $\epsilon(R_{90})$.
9. The planitude is determined as $\Pi = R_c/R_0$ and the mean alatitude as $\Lambda = \frac{1}{2}(R_{90+} + R_{90-})/R_0$. We also calculate an alatitude asymmetry as $\Delta\Lambda = \frac{1}{2}(R_{90+} - R_{90-})/R_0$. Note that in this paper we simplify the notation of Paper 0 by no longer using the prime symbol ($'$) to distinguish projected from intrinsic quantities. All planitudes and alitudes should be understood as specifying the projected bow shock shape on the plane of the sky unless noted otherwise.

After these automatic steps, we subjectively evaluate the resulting fit quality by giving a star rating to each source:

0 stars The fitting algorithm failed for some reason.

1 star The fit was formally successful, but the results for R_c or R_{90} are far removed from what a human would predict by looking at the image. For example, in the smallest bowshocks, which are only marginally resolved by Spitzer’s $6''$ beam, the dispersion in R_k can be a significant fraction of R_0 , in which case our algorithm tends to erroneously favor $R_c < R_0$.

2 stars The fit results are not totally outlandish, but nonetheless some problem is apparent that casts doubt on their reliability. For example, a double-shell structure to the bow shock that leads to large

differences between the “peak” and “mean” methods, or point sources near to the bow shock that interfere with the tracing procedure.

3 stars A good fit, but where the dispersion in R_k and/or the asymmetry in the bow shock reduces the precision in the determination of R_c and R_{90} , giving subjectively estimated uncertainties around the 20% level. An example of a 3-star fit is shown in Figure 2a.

4 stars A high quality fit, with subjectively estimated uncertainties in R_c and R_{90} around the 10% level. An example of a 4-star fit is shown in Figure 2b.

5 stars The highest-quality fit, usually corresponding to large, sharply defined bow shocks, whose shape is determined with high precision. An example of a 5-star fit is shown in Figure 2c.

Figure 2d compares the bow shock size, R_0 , determined by our fits (vertical axis) with the corresponding value given in the Kobulnicky et al. (2016) catalog (horizontal axis). For most sources with 3-star or higher rating, the two estimates agree to within $\pm 20\%$, but there are a small number of sources with a discrepancy of more than a factor of two. In all cases that we checked, we believe that our estimates of R_0 are more accurate than those in the catalog. It is apparent that the star ratings are correlated with the bow shock size, with larger bow shocks tending to receive higher ratings, although there is considerable overlap. In particular, most of the 1- and 2-star sources are close to the resolution limit of the MIPS GAL 24 μm images ($6''$, indicated by the dotted horizontal line in the figure).

In the following analysis, only those sources with a 3-star or higher rating are used. These comprise approximately half (227 out of 471) of all the MIPS GAL arc sources. In some cases of poor and failed fits, there is nothing apparently “wrong” with the source itself, and it is likely that minor tweaks to the methodology would improve matters, but we have elected not to do so, in order to maintain a uniform methodology across all sources.

The inset of Figure 2d shows histograms of the difference between the position angle, PA_0 determined by our fits and that listed in Kobulnicky et al. (2016). Although observational uncertainties undoubtedly contribute in part, the differences are mainly due to real asymmetries in the bow shocks, especially for the 4- and 5-star sources. The Kobulnicky et al. catalog PA_0 values are mostly sensitive to the orientation of the bow shock wings, whereas our fitted PA_0 values are determined by the point in the bow shock head that is closest to the stellar source. For this reason, we use the catalog PA_0 values for defining the axis when measuring R_{90+} and R_{90-} . On the other hand, the fitted values of PA_0 are better correlated with the position of the bow shock’s brightness peak, as is apparent in the lower left panels of Figure 2a and c.

2.2 OB bow shock shapes on the diagnostic plane

The derived bowshock shapes of all the 3-, 4-, and 5-star sources are shown in Figure 3 on the Π - Λ plane, which was discussed extensively in Paper 0. Figure 3a shows each individual source with horizontal error bars that represent the dispersion of traced points from the circle fit (step 7 of the previous section) and vertical error bars that show the wing asymmetry $\Delta\Lambda$ (step 9). The horizontal error bars, which are a proxy for observational uncertainties, become very small for the 4- and 5-star sources, whereas the vertical error bars remain at roughly the 10% level since they reflect real asymmetries in the shapes of the bow shocks.

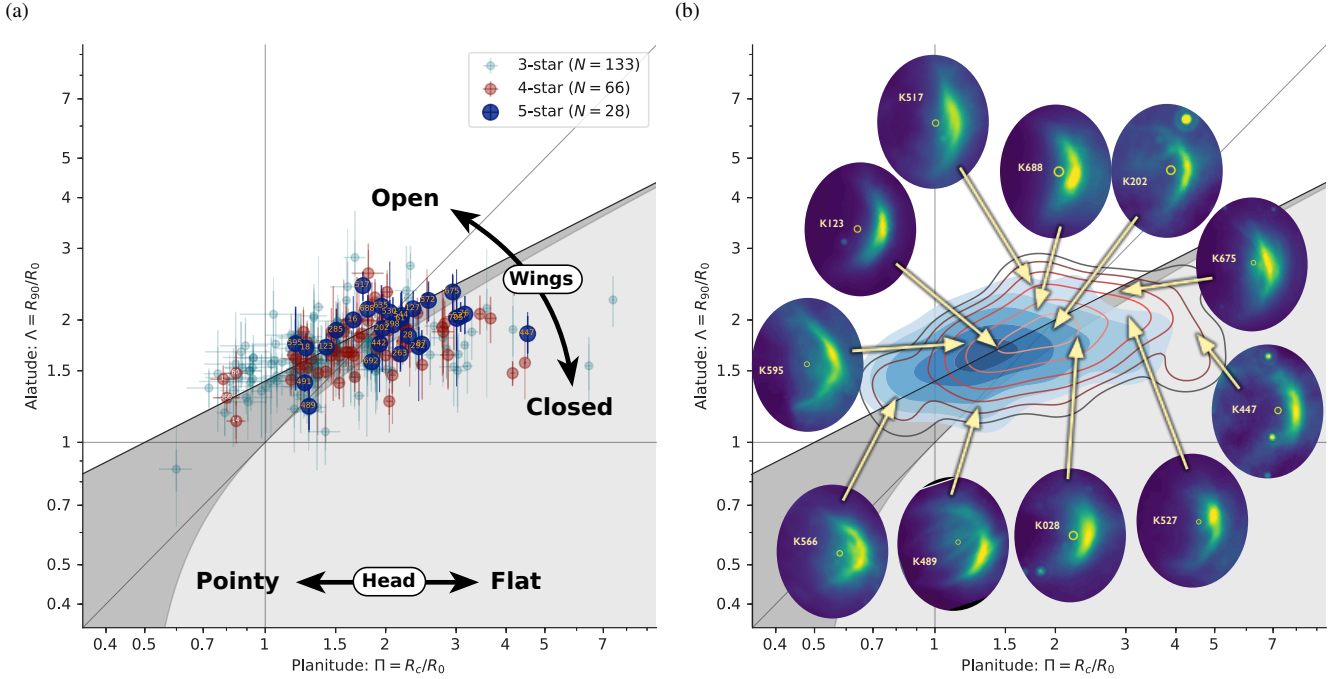


Figure 3. MIPS GAL sources on the bow shock shape diagnostic diagram of dimensionless radius of curvature versus perpendicular radius. The regions corresponding to different classes of quadrics are shown by shading (see § 4 of Paper 0): oblate spheroids (light gray background); prolate spheroids (darker gray background); paraboloids (black line); hyperboloids (white background). (a) Individual sources with bow shock fit quality rating of 3-star or above. All 5-star sources plus those 4-star sources with $\Pi < 1$ are labelled with their Kobulnicky et al. (2016) catalog number. Horizontal error bars do not directly reflect the uncertainty in Π but are instead simply the standard deviation from the circle fit of bowshock points R_k within $\pm 45^\circ$ of the axis. Values on the vertical axis represent the average of Λ_+ and Λ_- , with thin vertical error bars showing the difference between Λ_+ and Λ_- , and thick vertical error bars showing the rms dispersion of R_k about these values for bow shock points within $\pm 10^\circ$ of the $+90^\circ$ and -90° directions. (b) Kernel density estimator (KDE) of the distribution for 3-star sources (blue, filled contours) and 4- plus 5-star sources (orange/brown, unfilled contours). The KDE uses an anisotropic gaussian kernel with bandwidths of 0.06×0.04 in \log_{10} units. Thumbnail images of representative 4- and 5-star sources at different points on the Π - Λ plane are also shown. The angular scale of each image is indicated by a yellow circle of diameter $7.5''$, centered on the stellar source.

The horizontal axis corresponds to the shape of the head of the bow shock near its apex, ranging from sharper, pointier shapes with $\Pi < 1$ to flatter, snubber shapes with $\Pi \gg 1$, where it must be understood that all judgments of sharpness/flatness are with respect to the axial separation, R_0 , between the source and the bow shock apex (see Fig. 1). The vertical axis corresponds to the shape of the bow shock wings, ranging from closed “C” shapes for smaller values of Λ to open “V” shapes for larger values of Λ . The background shading shows the regions of the Π - Λ plane occupied by simple quadric shapes (see § 4 of Paper 0): oblate spheroids (light gray), prolate spheroids (dark gray), and hyperboloids (white). The boundary between closed and open corresponds to the paraboloids, and is shown by the solid line that divides the dark gray and white regions of the graph.

In Figure 3b, we present a smoothed version of the same data. The contours show the kernel density estimator (KDE, see Leiva-Murillo & Artés-Rodríguez 2012; Scott 2015) of the two-dimensional distribution of points on the Π - Λ plane. The KDE contours indicate that the distribution of 3-star sources is very similar to that of 4- and 5-star sources, although the higher-rated sources are shifted slightly to the upper right. Possible reasons for this are discussed in § 2.4 below. The bulk of the sources are concentrated around the paraboloid line, with $1 < \Pi < 3$, and $1.2 < \Lambda < 2$. But significant minorities are found in three other regions: (1) a clump with $\Pi \lesssim 1$; (2) a vertical spur towards higher Λ at $\Pi \approx 1.8$; and (3) a broad horizontal tail towards higher Π at $\Lambda \lesssim 2$. Thumbnail images of the $24\mu\text{m}$ emission of selected sources from different regions of the

distribution are shown, in order to illustrate the range of bow shock morphologies encountered.

2.3 Correlations between non-shape parameters of the OB sources

In Figure 4 we show the distributions over all MIPS GAL bow shock sources of the bow shock size, Galactic coordinates, extinction-corrected stellar source magnitude, and dust extinction. For the bow shock size, R_0 , we use the results from our model fitting rather than the values given in the Kobulnicky et al. (2016) catalog, but the distribution is very similar, as can be seen by comparing the top-left plot of Figure 4 with Kobulnicky et al.’s Figure 8.

The catalog gives the K -band extinction, A_K , derived using the method of Majewski et al. (2011). However, that assumes an intrinsic color of $(H - [4.5\mu\text{m}])_0 = +0.08$ magnitudes, which is too red if the sources are assumed to be OB stars. We therefore re-derive A_K from the catalog magnitudes combined with the Indebetouw et al. (2005) reddening law, but assuming $(H - [4.5\mu\text{m}])_0 = -0.1$ magnitudes, which is more typical of early type stars. This does not make very much difference (compare the top-right plot of our Fig. 4 with Kobulnicky et al.’s Fig. 9), but it does eliminate some of the apparent negative extinctions that are found in the catalog. The same reddening law gives $A_H = 1.55A_K$, and this is used to derive extinction-corrected H -band apparent magnitudes, H_0 .

The most significant linear correlation between any pair of parameters in Figure 4 is that between bow shock size and stellar

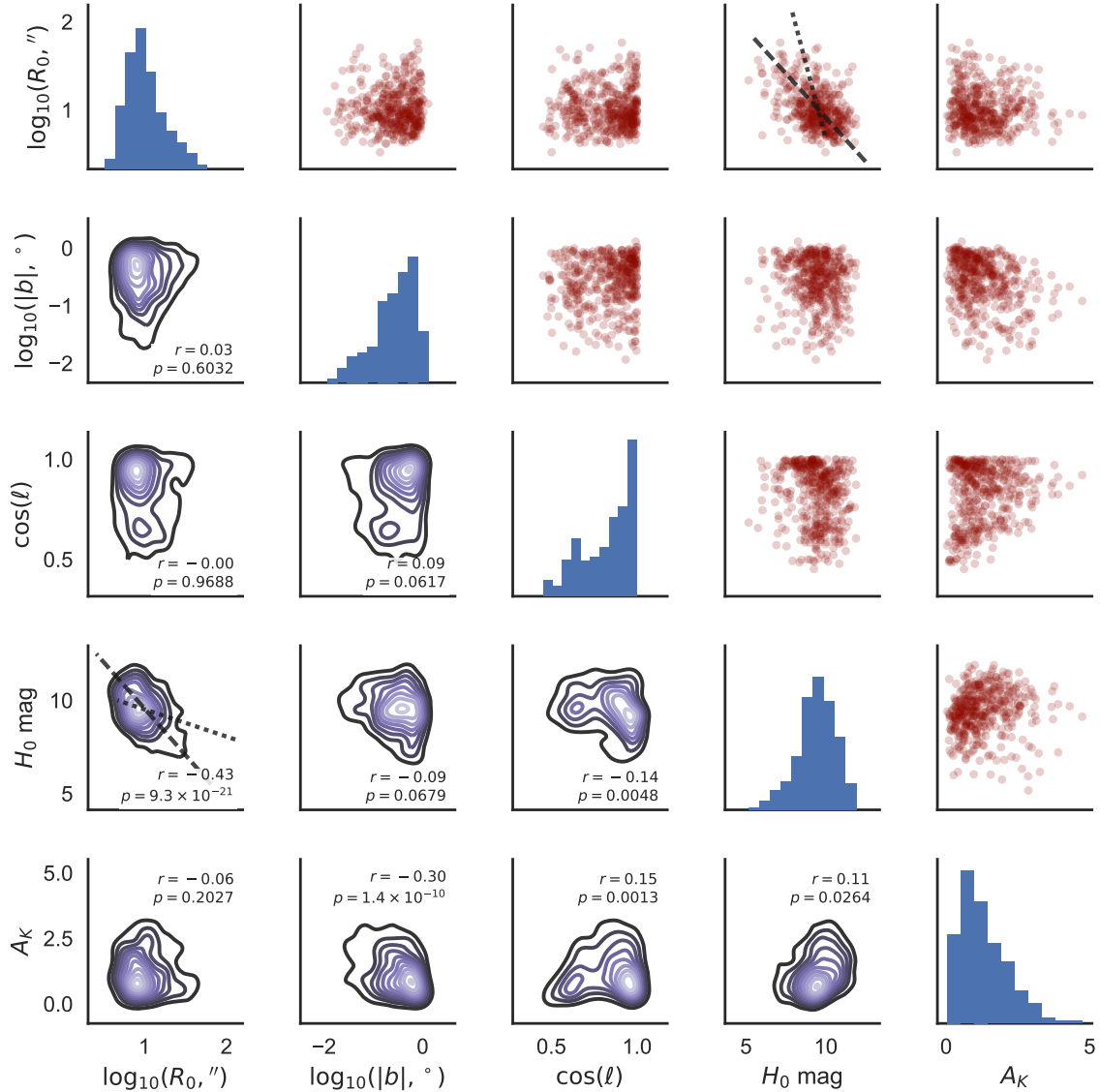


Figure 4. Matrix of pair plots that illustrate distributions of and correlations between the non-shape parameters of all MIPSGAL bow shock sources from Kobulnicky et al. (2016). Plots on the leading diagonal show histograms of the following parameters: bow shock angular size, $\log_{10} R_0$; Galactic latitude, $\log_{10} |b|$; Galactic longitude, $\cos \ell$; extinction-corrected H -band magnitude of the stellar source, H_0 ; K -band extinction, A_K . Scatter plots in the upper triangle show the joint distribution of each pair of parameters. These are repeated in the lower triangle but showing the KDEs of the joint distributions, which are annotated with the Pearson linear correlation coefficient, r , for each pair. The straight lines shown superimposed on the plots of stellar magnitude versus bowshock size correspond to toy model results for the same star at a sequence of distances (dashed lines) and a sequence of stellar luminosities at a fixed distance (dotted lines). See text for details.

source brightness: H_0 versus $\log_{10} R_0$, with correlation coefficient $r = -0.43$. The distribution of H_0 depends on the absolute magnitude, M_H , and the distance, d , to the source. It is likely that variation in d is the more important of the two because M_H changes relatively little for main-sequence OB stars, ranging from $M_H \approx -4$ (early-O) to $M_H \approx -1.5$ (mid-B). This is because part of the increase in bolometric luminosity, L , as one ascends the main sequence is offset by an increase in the effective temperature, T_{eff} , which shifts the peak of the stellar spectrum farther away from the H band, resulting in $L_H \propto L/T_{\text{eff}}^3 \sim L^{0.53}$, where the last step uses the upper main-sequence mass–luminosity and mass–radius scalings from Eker et al. (2015). It is true that evolved OB supergiants can be much brighter, reaching $M_H \approx -7$, but such stars are expected to be relatively rare. Assuming a B2V star ($M_H = -2$), then the observed range

$H_0 = 5\text{--}12$ corresponds to distances $d = 100\text{--}6300$ pc, and the histogram peak at $H_0 \approx 9.5$ corresponds to $d \approx 2000$ pc, which is all perfectly reasonable.

Turning now to the distribution of bow shock angular size, R_0 , this will also be affected by distance to at least some degree, since for a constant physical size the angular size will vary as $R_0 \propto d^{-1}$. For instance, if we assume that the physical size of all bow shocks is 0.1 pc and the absolute magnitude of all stars is $M_H = -2$, as above, then we find the relation $H_0 = 14.57 - 5 \log_{10} R_0$ if R_0 is measured in arcseconds. This is shown as a dashed line on the relevant panels of Figure 4 for values of R_0 that correspond to $d = 300$ pc to 8000 pc. It can be seen that this relation is in excellent agreement with the linear trend in the data. On the other hand, the correlation coefficient of $r = -0.43$ means in broad terms that only a fraction $r^2 \approx 20\%$

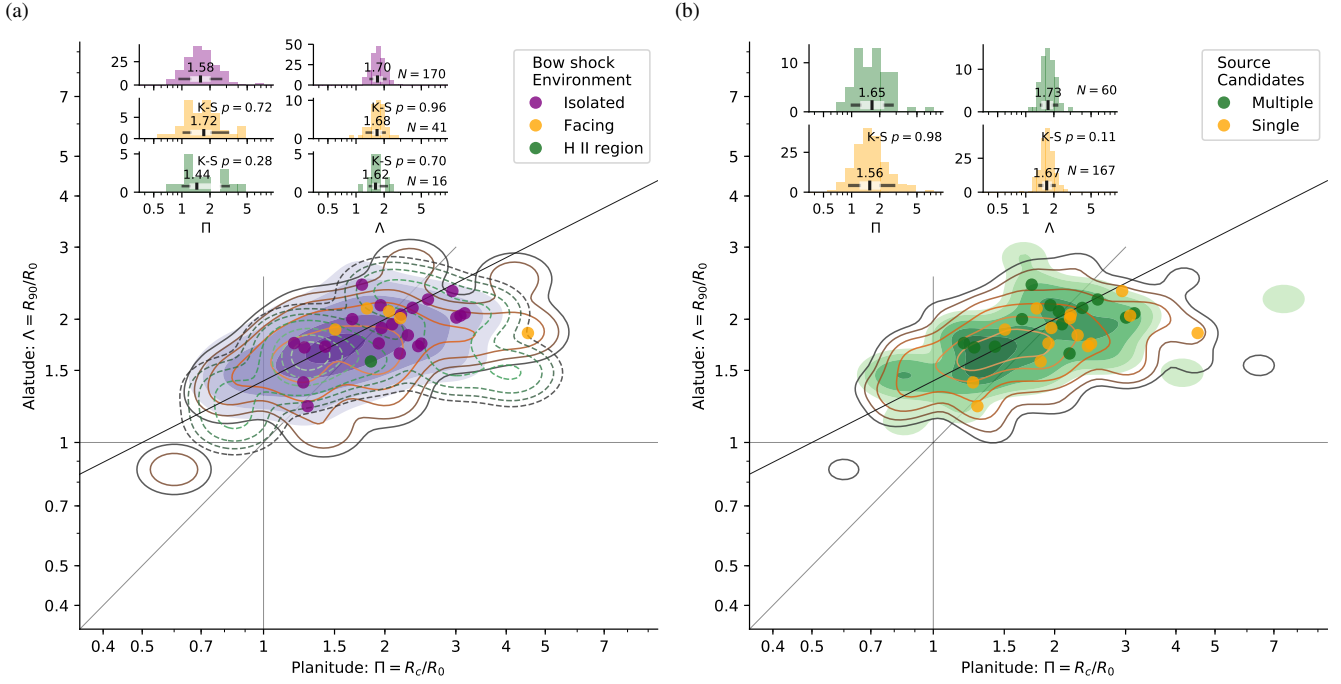


Figure 5. Example comparisons between the distribution of bowshock shapes when the sources are divided into two or more sub-samples according to the value of a categorical parameter. Contours show the KDE of the distribution of each sub-sample for all 3-, 4-, and 5-star sources, while filled circle symbols show 5-star sources only. Inset histograms show the marginal distributions on the two shape axes. (a) Source environment, divided into three sub-samples: “Isolated” (purple symbols and purple filled contours), “Facing H II region or 8 μ m bright-rimmed cloud” (orange symbols and orange-brown hollow continuous contours), and “Within H II region” (green symbols and green hollow dashed contours). (b) Uncertainty in stellar source identification, divided into two sub-samples: “Multiple candidates for stellar source” (green symbols and green filled contours) and “Single candidate for stellar source” (orange symbols and orange-brown hollow continuous contours).

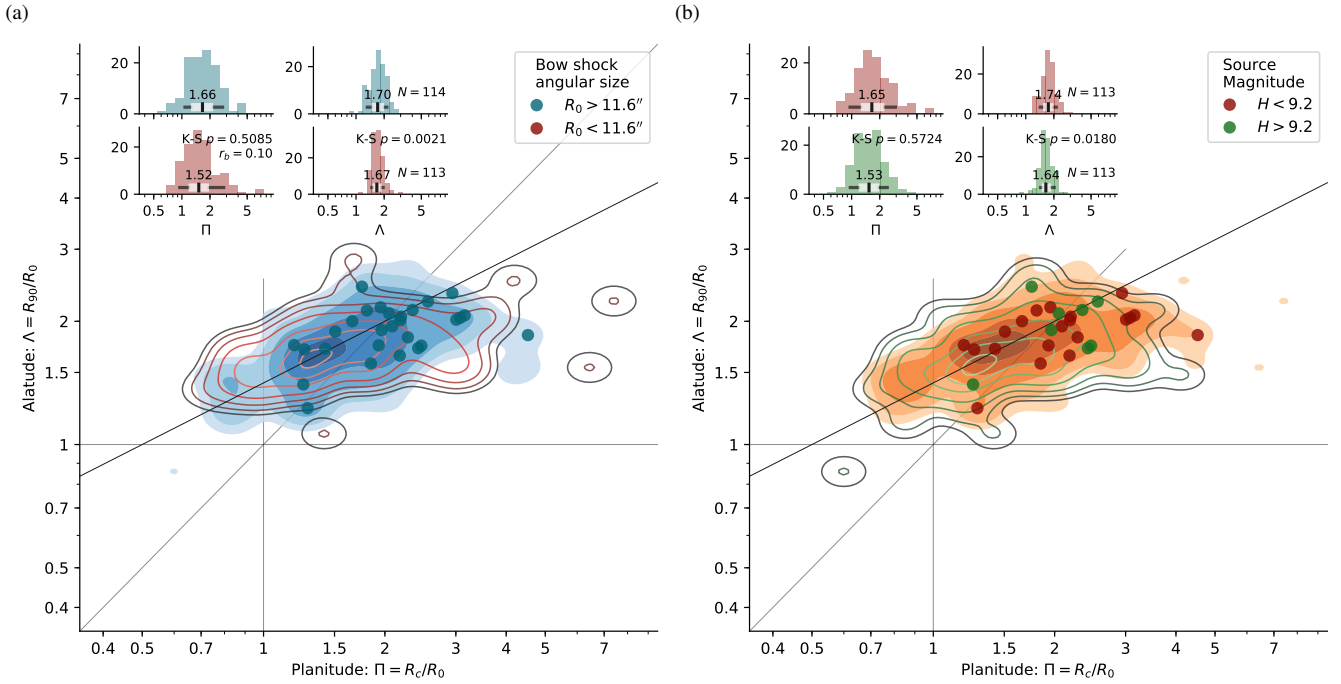


Figure 6. As Fig. 5 but for median splits of continuous parameters. (a) Bow shock angular size, R_0 , divided into two equal-sized sub-samples: large (blue symbols and blue filled contours) and small (red hollow contours). (b) Extinction-corrected H -band magnitude of the stellar source, divided into two equal-sized sub-samples: bright (red symbols and orange filled contours) and faint (green symbols and green hollow contours).

of the total variance in H_0 is “explained” by changes in R_0 , and vice versa, implying that one or both of H_0 and R_0 is only a very imperfect proxy for d . We have already seen that the spread in H_0 probably is mostly due to a spread in distance, rather than a spread in H -band stellar luminosity. If this is true, it follows that it is R_0 that depends only weakly on d and is more influenced by other factors.

One such factor is the stellar/environmental momentum-loss ratio, β , between the two supersonic flows that form the bow shock. All other things being equal, we have $R_0 \propto \beta^{1/2}$ for $\beta \ll 1$, as is typically the case. If the environment flow is constant and the OB star wind has mass-loss rate \dot{M} and terminal velocity V_∞ , then $\beta \propto \dot{M}V_\infty$. Empirical and theoretical studies of hot star winds (e.g., Puls et al. 1996) imply $\dot{M}V_\infty \sim L^{1.88}R^{-1/2} \sim L^{1.80} \sim L_H^{3.40}$, where the final two steps apply only to main-sequence stars and again use the relations of Eker et al. (2015). If we assume as above that a B2V star with $M_H = -2$ has a bow shock physical size of 0.1 pc, and consider a sequence of stars with varying H -band luminosities but all at a fixed distance of $d = 2000$ pc, then we find the relation $H_0 = 8.02 - 1.49 \log_{10} R_0$. This is shown as a dotted line in the relevant panels of Figure 4 for the absolute magnitude range $M_H = -3.6$ (O6V) to $M_H = -1.5$ (B5V). It can be seen that this relation does not match the linear trend in the data, and predicts a much larger spread in R_0 over a narrow range in H_0 than is observed. This could mean one of two things: first, it may be that the range of stellar luminosities is significantly narrower than we have supposed, implying that B stars vastly outnumber O stars among the sources. Alternatively, there may be a positive correlation between the stellar luminosity and the momentum of the environmental flow, with the result that β varies less steeply with L_H than we have assumed. That could arise if more luminous stars were preferentially found in denser environments, or, in the case of runaways, if more luminous stars tended to be faster moving.

A third factor that may influence R_0 is the inclination, i , of the bow shock axis with respect to the plane of the sky. Figure 11b of Paper 0 shows that for $\Pi > 1$, then the projected R'_0 becomes larger than the true R_0 as $|i|$ increases (see also Figs. 26 and 27 of Paper 0). It can be seen that the effect is relatively modest, with an increase in R_0 of no more than a factor of 2 to 3.

2.4 Correlation between bow shock shape and other parameters

We now investigate if the bow shock shapes of the MIPS GAL sources are correlated with any other parameters via the following methodology:

1. For each of the parameters in the Kobulnicky et al. (2016) catalog, we divide the sources into two or more sub-samples, according to the value of the parameter. For quantitative parameters, such as those discussed in the previous section, we use two sub-samples of equal size, with membership determined by whether the parameter is larger or smaller than the median value. But we also use categorical parameters, such as the type of bow shock environment, or the presence/absence of $8 \mu\text{m}$ emission, in which case the sub-samples are of unequal size.
2. We plot the KDEs of the two sub-samples separately on the Π – Λ plane (see Figs. 5 and 6) to check for any obvious differences.
3. We check if there is any statistically significant difference between the bow shock shapes of the sub-samples by applying three different non-parametric tests to Π and Λ separately.

The principal test used is Kuiper’s variant of the two-sample Kolmogorov–Smirnov test (e.g., Stephens 1970; Pal-

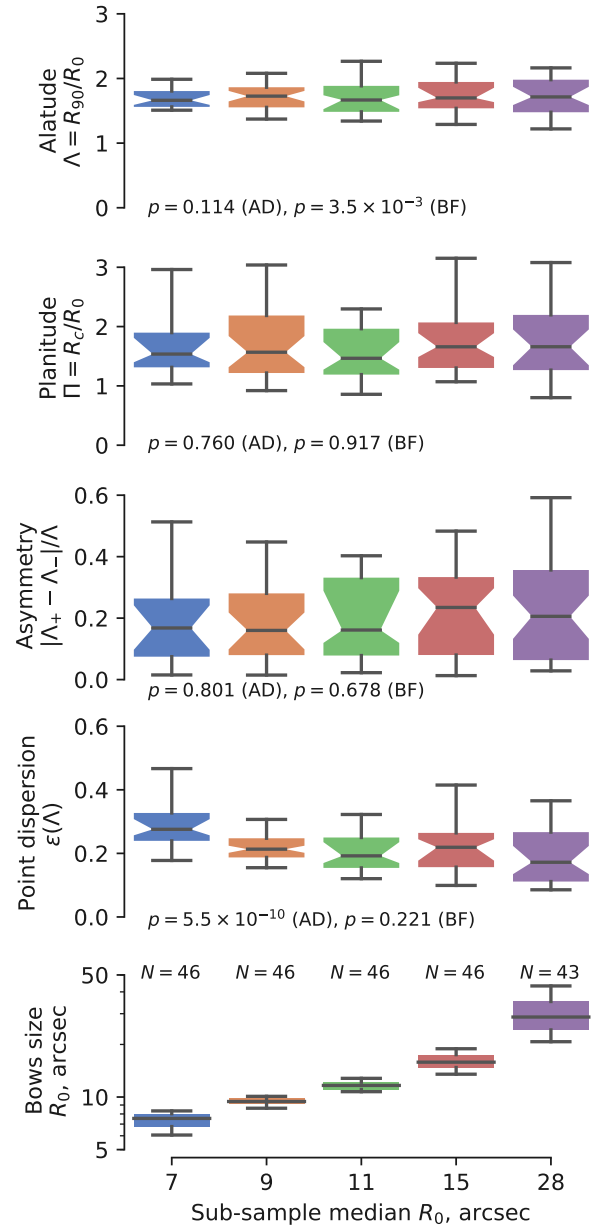


Figure 7. Box plots of the distributions of bow shock shape parameters, Π and Λ , together with a measure of the tail asymmetry, $2|\Delta\Lambda|/\Lambda$, after partitioning on the bow shock size, R_0 . All 3-, 4-, and 5-star sources are sorted according to R_0 and divided into 5 non-overlapping sub-samples of roughly equal size, each labelled by their median value of R_0 in arcseconds, as illustrated in the lower panel. The colored boxes show the interquartile range of the data, with the median indicated by a horizontal line and the notch showing the 90% confidence limits of the median, as determined from 1000 bootstrap resamplings. The 5th-to-95th centile range of the data is indicated by error bars. A 5-sample Anderson–Darling test and Brown–Forsythe test is performed for each dependent variable, with resultant p -value given at the bottom of each panel. It is apparent that the dispersion in Λ (upper panel) increases systematically with R_0 , although the central value is roughly constant. No clear systematic changes are apparent in Π (second panel).

tani 2004), as implemented by the Python library function `astropy.stats.kuiper_two` (Astropy Collaboration et al. 2018). This is a general test of the *null hypothesis* that the two sub-samples are drawn from the same distribution. It returns a p -value, which is the estimated probability that the observed difference between the two sub-samples would be as large as it is purely by chance if they were all were drawn from the same distribution. We consider two different thresholds for significance: $p < 0.05$ (approximately $2\text{-}\sigma$ for a normal distribution) and $p < 0.003$ (approximately $3\text{-}\sigma$). We show in Appendix A that, given the large number of potential relationships that we are testing, the more stringent $p < 0.003$ condition is required in order to confidently reject the null hypothesis and declare a “significant” difference between the two sub-samples, but we also consider the less strict threshold of $p < 0.05$ as an indicator of “possible” difference. We supplement the general-purpose Kuiper test with two tests that probe specific features of the sample distributions: the Mann–Whitney–Wilcoxon U test (Mann & Whitney 1947), which is sensitive to differences in the central value (e.g., median) and the Brown–Forsythe test (Brown & Forsythe 1974), which is sensitive to differences in the variance, or width, of the distribution (see Appendix A for details).

As shown in detail in Table A1, there is remarkably little variation in the bow shock shape distributions as a function of most of the other parameters. Two examples in which there is *no* significant shape difference between the sub-samples are shown in Figure 5. This lack of difference is interesting because in both examples there are a priori grounds to suspect that differences might exist. The first example (Fig. 5a) is the bow shock environment, which was categorized in Kobulnicky et al. (2016) as “Isolated” (I), “Facing a large H II region” (FH), “Facing a $8\text{ }\mu\text{m}$ bright-rimmed cloud” (FB), and “Within a giant H II region” (H), and where we have merged the FH and FB categories, labelled “Facing” in the figure.² The shapes might be expected to vary with environment because the FB and FH categories should be associated with “weather vane” interactions (Povich et al. 2008) between the stellar wind and a divergent photoevaporation flow. This is expected to give a more open bow shock than in the “runaway” case of interaction of a moving star with a static environment. In the thin-shell approximation, the predicted shapes are a cantoid for weather vanes and a wilkinoid for runaways, see § 6 of Paper 0. The fact that no such difference is detected could be explained in one of two ways: (i) the momentum ratio β for the weather vanes could be small, since the cantoid becomes indistinguishable from the wilkinoid as $\beta \rightarrow 0$, or (ii) many of the bow shocks classified as “Isolated” might also be weather vanes rather than runaways.

The second example (Fig. 5b) divides the sources according to whether or not Kobulnicky et al. (2016) judged there to be multiple candidates for the identity of the central star that drives the bow shock. If the central star were to be misidentified in a significant number of sources, then the measured value of R_0 for those sources would be erroneous, which would increase the scatter in both Π and Λ . The fact that no significant difference is seen in the shape distributions between sources with/without multiple candidates implies that such mistakes in identification of the central star must be rare.

We also tested all the other source parameters listed in Kobulnicky et al.’s catalog, finding no significant shape differences for sources with/without $8\text{ }\mu\text{m}$ emission, with low/high extinction, closer/farther from the Galactic plane, or closer/farther from the Galactic center. Details are given in Table A1. In all these cases,

differences in mean or median Λ less than 0.06 and in Π less than 0.16 are found, corresponding to rank biserial correlation coefficients (a non-parametric dimensionless measure of the difference between two samples, see Appendix A) of $r_b < 0.15$, which are not significant even at the $2\text{-}\sigma$ level.

The only parameters that *do* show a possible correlation with the bowshock shape are the bow shock angular size, R_0 , and the extinction-corrected magnitude of the central star, H_0 , which are illustrated in Figure 6. The general purpose Kuiper test indicates differences in the sub-sample distributions of Λ at the $2\text{-}\sigma$ level for H_0 and at the $3\text{-}\sigma$ level for R_0 . It is apparent from the histograms shown in the right-hand inset graphs of Figure 6a that in the case of the small/large R_0 sub-samples it is the width rather than the central tendency of the distributions that is different, which is confirmed by the more specific Brown–Forsythe test, which indicates a difference between the sub-sample dispersions at the $3\text{-}\sigma$ level. In the case of the faint/bright H_0 sub-samples (Fig. 6b), it is less clear what feature of the distributions differ.

In order to investigate these effects in more detail and look for systematic trends, we divide the independent parameter (R_0 or H_0) into 5 rather than 2 equal-sized sub-samples, with results in the case of R_0 shown as box plots in Figure 7. This time the k -sample Anderson–Darling test (Anderson & Darling 1952; Scholz & Stephens 1987; Makarov & Simonova 2017) is used to determine the statistical significance of any observed differences. A systematic increase with R_0 in the dispersion of Λ (upper panel of Fig. 7a) is apparent from both the interquartile range (colored boxes) and interdecile range (error bars). As a check on whether observational uncertainties might be contributing to this trend, the third and fourth rows of box plots show the statistics for, respectively, the fractional asymmetry of the bowshock wings and the standard deviation, $\epsilon(\Lambda)$, of the individual points on the bow shock that go into determining Λ (see step 8 of the tracing/fitting methodology described in § 2.1). It can be seen that neither of these quantities tends to increase with R_0 , and in fact there is a significant *decrease* in $\epsilon(\Lambda)$ with R_0 . This implies that the increase with angular size of the diversity of bow shock wing shapes is real, and not due to observational uncertainties. On the other hand, we find that no clear trends are evident as a function of source magnitude H_0 (not illustrated), which leads us to suspect that the $p < 0.05$ result obtained for the 2-sample Kuiper test was a *false positive*, as is also supported by the analysis in Appendix A and Figure A1.

As mentioned in § 2.2 there is also a shape difference between the 3-star sources and the 4/5-star sources (see Fig. 3b). The p -values of statistical tests (see Table A1) indicate that this is much more significant than any correlation with the other parameters discussed in this section ($p < 10^{-4}$ for Λ and $p < 10^{-5}$ for Π). This means that it cannot be simply due to the tendency of the higher-rated sources to have larger angular sizes. However, the subjective nature of the star ratings makes this result hard to interpret.

3 FAR-INFRARED ARCS AROUND LATE-TYPE STARS

We obtain a second sample of bow shocks from a far-infrared survey (Cox et al. 2012) of circumstellar shells around known asymptotic giant branch (AGB) stars and cool supergiants, obtained as part of the *Herschel* MESS (Mass-loss of Evolved StarS) program (Groenewegen et al. 2011). The survey sources were divided into four classes by Cox et al., according to the overall shape of the extended emission at $70\text{ }\mu\text{m}$ (see their Table 4): “fermata \curvearrowright ”, or arcs (Class I); “eyes \odot ” (Class II); “rings \odot ” (Class III), and

² Similar results are also found for the FB and FH categories separately.

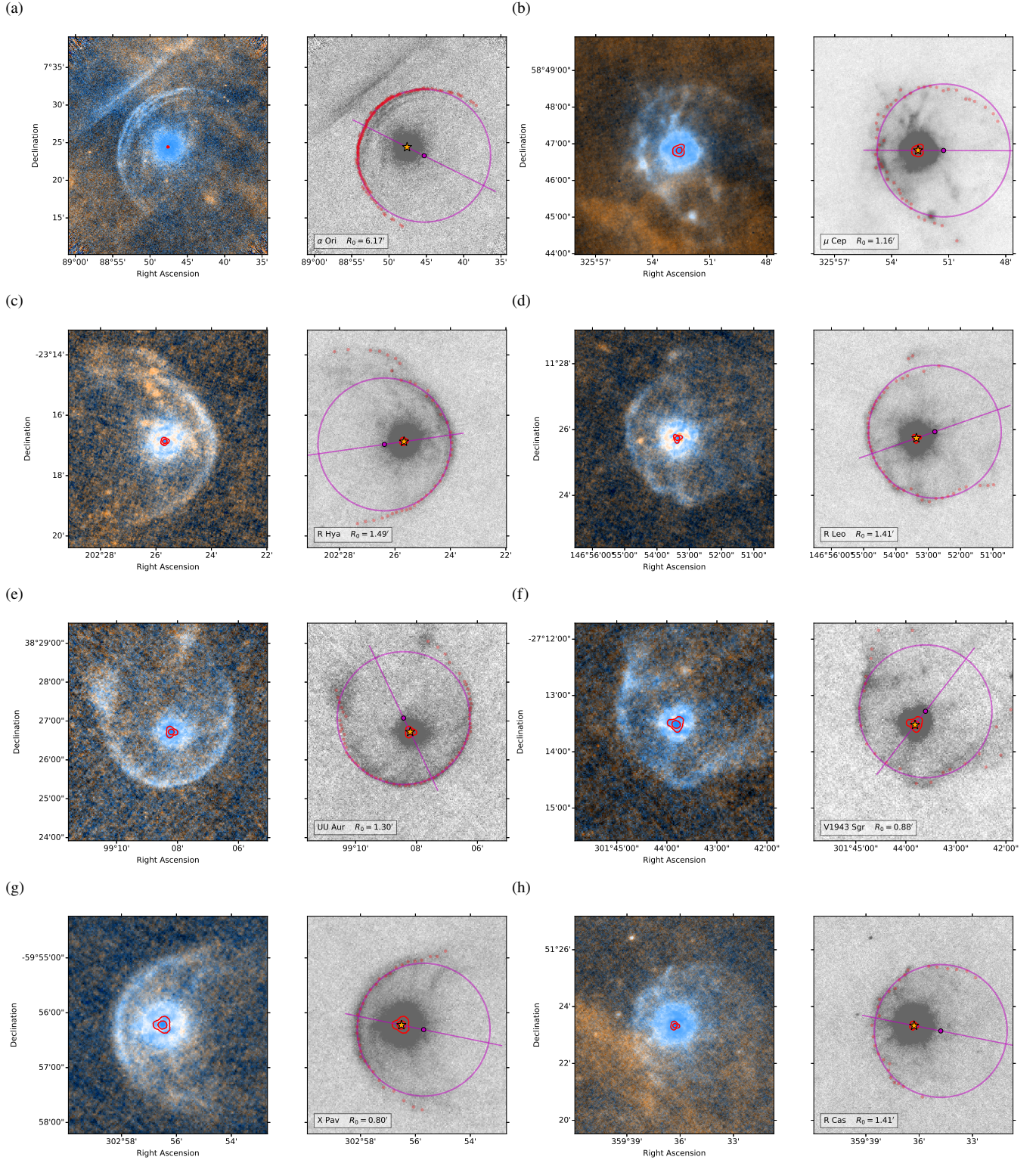


Figure 8. RSG and AGB shells observed with Herschel. Selected Class I sources (“fermata-like”) from the MESS survey Cox et al. (2012), where the arc structure is particularly clear and symmetrical. Left panels show PACS 70 μm surface brightness (blue) and 160 μm (orange). Right panels show tracing of the bow shock arc (red symbols) and circle fit (magenta lines and symbols) superimposed on a low-contrast image of the 70 μm surface brightness. (a) α Ori. (b) μ Cep. (c) R Hya. (d) R Leo. (e) UU Aur. (f) V1943 Sgr. (g) X Pav. (h) R Cas.

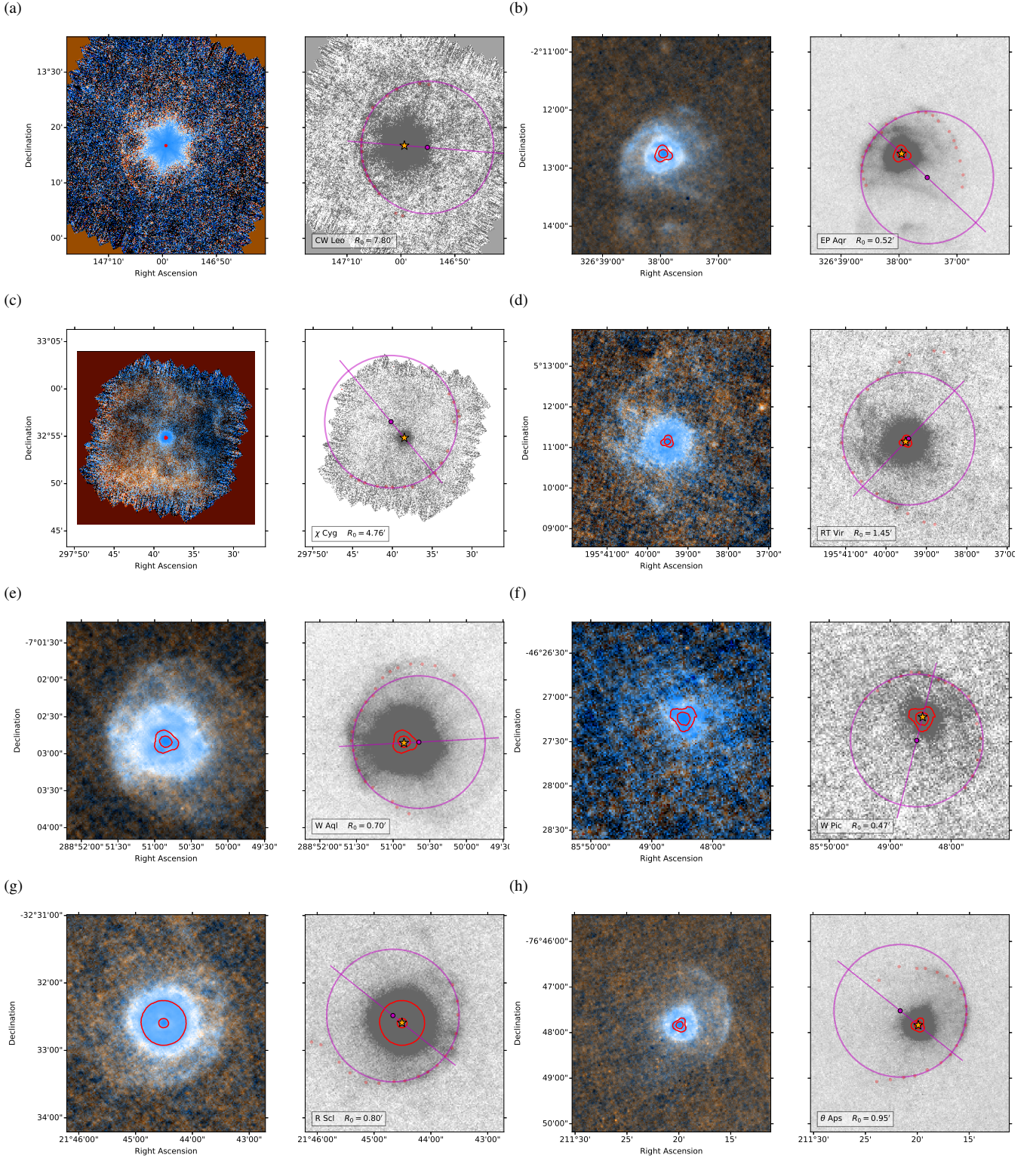


Figure 9. As Fig 8, but for a further 8 Class I sources from Cox et al. (2012) where the arc structure is more diffuse, weak, and/or asymmetric. (a) CW Leo. For this source only, the right-hand panel shows a grayscale image of the 160 μ m rather than 70 μ m emission. (b) EP Aqr. (c) χ Cyg. (d) RT Vir. (e) W Aql. (f) W Pic. (g) R Scl. (h) θ Aps.

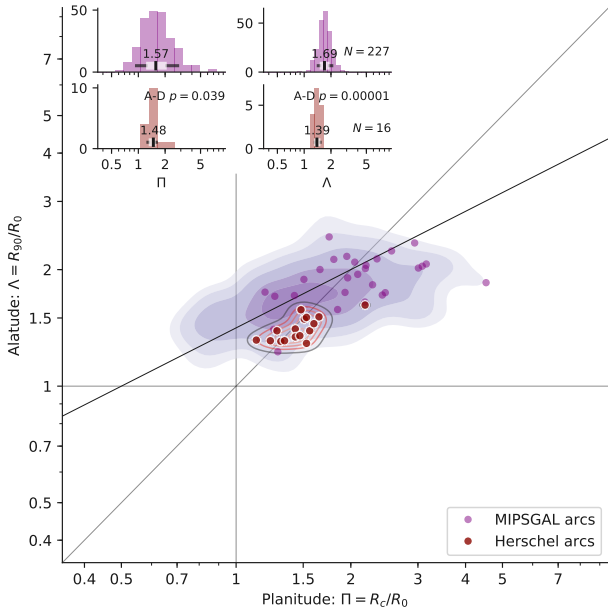


Figure 10. Comparison of bow shock shapes between Herschel RSG/AGB arcs (large red symbols and hollow red contours) and MIPS GAL OB star arcs (small purple symbols and filled purple contours). Other details of the plots are as in Figs. 3, 5, and 6.

“irregular” (Class IV). Of these, only the Class I sources clearly correspond to bow shocks, which represent 22 out of 50 total sources detected with extended emission. For our sample, we select the 16 Class I sources where the shape parameters can be reliably measured, and which are shown in Figures 8 and 9. The remaining six Class I sources (Fig. 1 of Cox et al. 2012) are too asymmetrical or irregular to reliably determine R_c and R_{90} , and are therefore excluded from our sample.

In most sources, the bow shock shell is most clearly visible in the $70\,\mu\text{m}$ band, with the exception being CW Leo where the $180\,\mu\text{m}$ band is used instead. In several sources, the shell is split into multiple filaments, with the clearest example being α Ori (Betelgeuse), shown in Figure 8(a). For such sources, we take the outer envelope of the filaments as the bow shock arc. Given this complication, and the fact that the angular resolution relative to the bow shock size is much better than in the MIPS GAL sources, we judge that the arc tracing is best performed by eye and this is carried out using the SAOImage DS9 FITS viewer (Joye & Mandel 2003), with results shown as small red open circles in Figures 8 and 9 (more details of this technique are given in §§ 6 and 7 of Paper 0). Subsequently, the bow shock parameters R_0 , Π , and Λ are determined by circle fits, as in steps 5–9 of § 2.1, with results shown in magenta on the figures.

Figure 10 compares the distributions of bow shock shapes between the Herschel (RSG/AGB) and MIPS GAL (OB star) samples. The Kuiper test gives a highly significant difference between the Λ distributions of the two samples, but only a marginally significant difference between the Π distributions (detailed results are shown in Table A1). The Herschel sources show considerably smaller alatitude (median $\Lambda \approx 1.4$), implying bow shock wings that are more closed than in the MIPS GAL sources (median $\Lambda \approx 1.7$). For the planitude, there is only a slight difference in average values: median $\Pi \approx 1.5$ for Herschel versus ≈ 1.6 for MIPS GAL, which is not statistically significant (rank biserial $p = 0.29$). On the other hand, the dispersion in Π is four times smaller for the Herschel sample,

which is marginally significant (Brown–Forsythe $p = 0.015$). In particular, the MIPS GAL sample shows a substantial minority of very flat-nosed shapes ($\Pi > 2$), but these are absent in the Herschel sample. The same can be seen directly by comparing the RSG/AGB bow shock shapes in Figures 8 and 9 with the representative OB bow shocks of Figure 3b. The MIPS GAL sources K489 and K123 have shapes that are similar to specific Herschel sources (UU Aur and R Hya, respectively), while sources such as K447 (extreme flat head) or K517 (extreme open wings) have no analog among the Herschel sources.

4 STATIONARY EMISSION LINE ARCS IN M42

We obtain a third sample of bow shocks from a catalog of stationary emission line arcs in the Orion Nebula (Bally et al. 2000), which are detected via their $H\alpha$ emission in HST ACS surveys of the nebula (Bally et al. 2006; Robberto et al. 2013). Out of a total of 73 such objects (Gutiérrez-Soto 2015) we have selected 18 where the observations are of sufficient quality to reliably measure the planitude and alatitude. Images in the ACS f658n filter of these sources are shown in Figure 11. Some of the sources were identified as LL Orionis-type objects by Bally & Reipurth (2001) and are identified as LL 1–6. The remaining sources are labeled by their coordinate-based designation according to the system of O’Dell & Wen (1994). The determination of the bow shock shape for each source was carried out as described in § 7 of Paper 0, using the “ridge” method for manually tracing the arc (see Fig. 28 of Paper 0). In some sources, such as LL 1, LL 6, 109–246, and 4468–605, a high-velocity jet flow is also seen to issue from the star (Bally et al. 2006; Henney et al. 2013). We took care when tracing the arcs of such sources to avoid regions where jet knot emission is projected on the bow shock shell.

The planitude and alatitude are found by circle fitting using the algorithm described in Paper 0’s Appendix E, as implemented in the python program `circle-fit.py`.³ The only adjustable parameter of the algorithm is $\Delta\theta$, the maximum angle from the bow shock axis of points that are included in the circle fit. We tested all values of $\Delta\theta$ in 5° increments from 45° to 80° and found that $\Delta\theta = 55^\circ$ to 70° gives stable results for all sources. The accuracy of the fitted planitudes can be estimated from the dispersion in values of Π for the same source with different $\Delta\theta$, which we find to be $\approx 10\%$. The fitted alitudes have a much smaller dispersion $\approx 1\%$, but in this case the accuracy is limited by the asymmetry of the wings, as characterized by $\Delta\Lambda/\Lambda$ with an RMS value of $\approx 15\%$.

The resultant shape distribution for the Orion Nebula arcs is shown in Figure 12, where it is compared with the OB star shapes from § 2.2. It can be seen that both the planitude and alatitude distributions are shifted towards higher values, with median values of $\Pi = 2.70$ and $\Lambda = 2.55$. The difference from the MIPS GAL sources ($\Pi = 1.57$ and $\Lambda = 1.69$) is highly statistically significant, as indicated by extremely low p -values for the Kuiper tests. It is also at least 4 times larger than the systematic fitting uncertainties discussed in the previous paragraph. On closer inspection, it appears that the shape distribution is bimodal. Four of the sources (005–514, 4468–605, 116–3101, 308–3036) are similar to typical OB stars, with $\Lambda \approx \Pi \approx 1.5$, whereas the remainder are concentrated in the range $\Pi = 2$ to 4, with an extended tail towards higher planitude. The alitudes mainly follow the line for parabolas, $\Lambda = (2\Pi)^{1/2}$ (see

³ <https://github.com/div-B-equals-0/circle-fit>

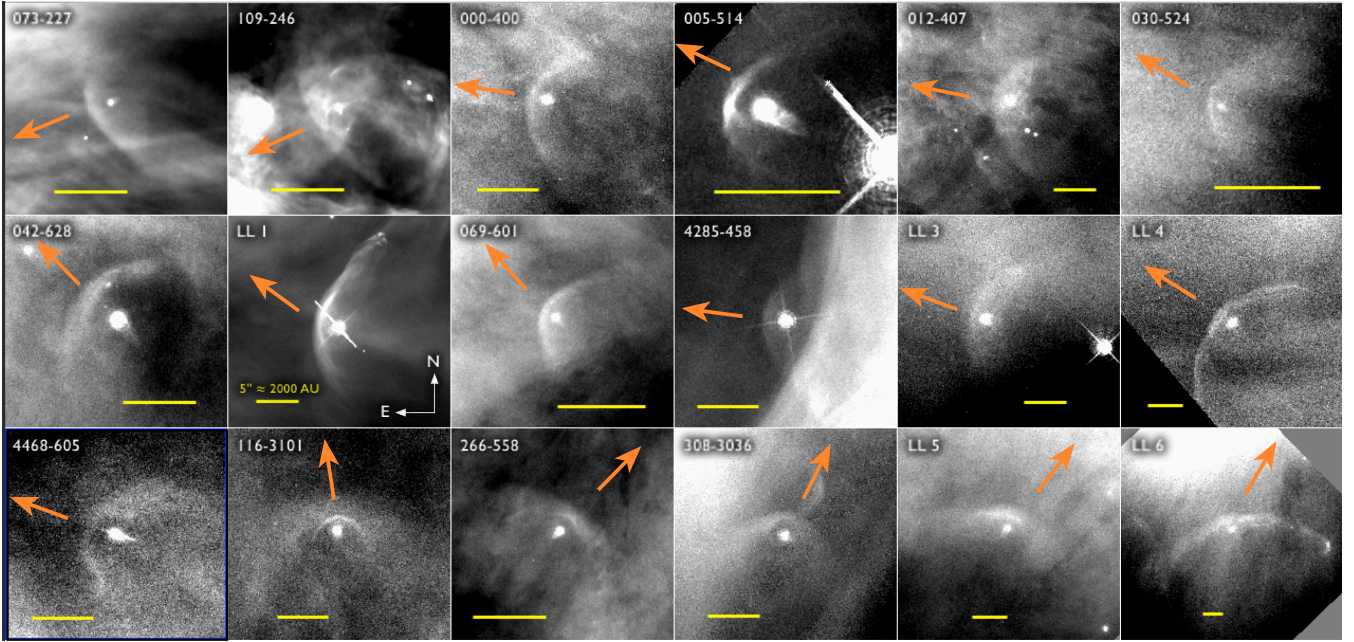


Figure 11. Stationary bow shock arcs in the Orion Nebula. Images are of $H\alpha$ plus $[N II]$ emission through the HST ACS f658n filter. The angular scale of each image is different, with the yellow horizontal lines indicating $5''$, corresponding to a physical scale of ≈ 0.01 pc. Orange arrows indicate the direction to the principal ionizing star, θ^1 Ori C.

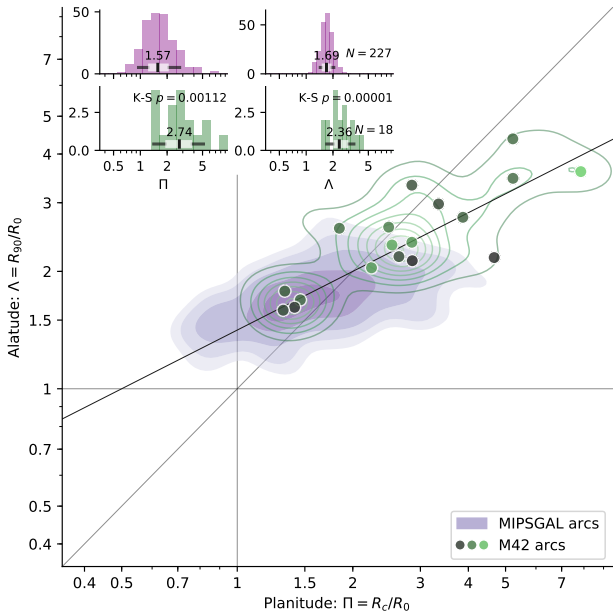


Figure 12. Shape comparison between Orion Nebula arcs (green) and OB star bow shocks (purple). Other details of the plots are as in Figs. 3 and 5, except that a larger KDE smoothing bandwidth of 0.06×0.045 is used for the Orion Nebula sample. The colors of the individual points for the Orion Nebula sample show the size-to-distance ratio, R_0/D , on a logarithmic scale from $R_0/D = 0.002$ (dark green) to $R_0/D = 0.018$ (light green).

App. C of Paper 0), and the deviations from this line can be readily understood in terms of peculiar morphologies of the source (Fig. 11). For instance, LL 4 and 266–558 both show large alitudes for their respective planitudes and these are both sources where the bow shock wings seem to bend outwards instead of following the curve

from the apex region. In contrast, 030–524 has a small alitude for its planitude and this is a very asymmetric source with an apparent corner to the shell on one side.

Uniquely among the three bow shock datasets, for the Orion Nebula arcs we know the source of the external flow. This is not the stellar wind from the high-mass stars at the center of the cluster, which has insufficient momentum at the position of the arcs (Bally et al. 2000), nor is it due to stars’ own motions, since the space velocities of all these sources are very low, conforming to the velocity dispersion $\sigma_{1D} \approx 2 \text{ km s}^{-1}$ of the Orion Nebular Cluster (Dzib et al. 2017; Kim et al. 2018). Instead it is due to the transonic champagne flow of photoionized gas away from the core of the nebula (Zuckerman 1973; Henney et al. 2005), which has its density peak in the Orion S region (Weilbacher et al. 2015), located roughly $30''$ SW of the dominant Trapezium star θ^1 Ori C. The bow shock sources are located at much larger distances of $D = 90''$ to $700''$ from θ^1 Ori C, so that the ratio R_0/D can be used as a proxy for the local divergence of the champagne flow on the scale of the bow shock (notice that the symmetry axes of the bow shocks in Fig. 11 are always roughly parallel to the direction to θ^1 Ori C). This is indicated by the color of the points in Figure 12, with lighter colors corresponding to a larger R_0/D and hence a more divergent external flow. It can be seen that there is some correlation between the bow shock shapes and R_0/D : the source with the largest Π , 109–246, also has the largest R_0/D , while the four sources with low Π and Λ all have low R_0/D . However, the correlation is far from perfect, with a Pearson correlation coefficient of only $r = 0.47$.

5 DISCUSSION

In this section, we discuss the physical implications of our empirical findings regarding bow shock shapes. Our most reliable result is the average shape of the OB bow shocks from the 227 MIPSGAL sources with quality rating of 3 stars or higher. This yields mean

values of $\Pi = 1.78 \pm 0.06$ and $\Lambda = 1.72 \pm 0.02$, or median values of $\Pi = 1.57$ and $\Lambda = 1.69$. The uncertainty quoted on the mean values is the “standard error of the mean”: $\text{sem} = \sigma/\sqrt{n}$, where σ is the rms dispersion and n is the number of sources. Note that in the case of the planitude $\text{sem}(\Pi) = 0.06$ is considerably smaller than $\text{mean}(\Pi) - \text{median}(\Pi) = 0.21$, so the latter would be a more conservative estimate of the uncertainty.⁴ These values can be compared with the predictions of the thin-shell wilkinoid model (Wilkin 1996), which are $\Pi = 1.67$, $\Lambda = 1.73$ when the bow shock axis lies in the plane of the sky (following Paper 0, this is defined as the zero point of the inclination angle, i). When the axis is inclined, both planitude and alatitude are predicted to decrease but not by very much, tending to $\Pi = 1.5$, $\Lambda = 1.63$ as $|i| \rightarrow 90^\circ$ (see § 5.3 of Paper 0). The median observed value falls squarely inside this range for both the planitude and alatitude, which is a remarkable triumph for the Wilkin (1996) model.

5.1 Diversity in bow shock shapes

On the other hand, turning now to the *variety* of bow shock shapes, we see that the wilkinoid can no longer explain our results. The rms dispersions of the planitude and alatitude distributions for the MIPS GAL sources are $\sigma(\Pi) = 0.87$ and $\sigma(\Lambda) = 0.30$ (Tab. A1), which are respectively 5 times and 3 times larger than the total range of variation of Π and Λ predicted for the wilkinoid surface. Although some of the dispersion is due to uncertainties in the observations and the fitting algorithm, this contribution is expected to be small, especially for the larger, well-resolved sources, for which systematic uncertainties in the methods for determining Π and Λ will dominate. Conservative upper limits to the relative size of these uncertainties were estimated in § 7 of Paper 0 to be $< 20\%$ for Π and $< 10\%$ for Λ , whereas the observed dispersions are roughly twice as large: $\sigma(\Pi)/\Pi = 55\%$ and $\sigma(\Lambda)/\Lambda = 18\%$. Furthermore, the variations in planitude and alatitude are readily apparent by eye, as is demonstrated by the example bow shock images shown in Figure 3b. Sources such as K123 have very typical shapes and fall near the center of the Π – Λ distribution, whereas high- Π sources such as K447 have a very flat apex region, while low- Π sources such as K566 have a pointier, almost triangular apex. High- Λ sources, such as K517, have very open wings that bend away from the star, while low- Λ sources such as K489 have closed wings and a semi-circular appearance.

5.1.1 The influence of projection effects

In Paper 0 we found that certain bow shock shapes can show a much greater variation in their projected appearance as a function of inclination angle than is seen for the wilkinoid. For example, the cantoids and ancantoids, which have asymptotically hyperbolic far wings, can shift towards higher apparent planitude and alatitude as the inclination increases, generally with $\Lambda \geq \Pi$ (Fig. 20 of Paper 0). This might plausibly explain the vertical spur towards higher Λ seen in the empirical distribution (§ 2.2). A different behavior is shown by bow shocks with very flat apex regions, such as the MHD simulation from Meyer et al. (2017) that is analyzed in the § 6 of Paper 0. This shows a high planitude Π when the orientation is exactly edge-on, but Π decreases sharply along a roughly horizontal track as the inclination $|i|$ increases (Fig. 25 of Paper 0). This is similar to the principal axis of variation of the observed shapes (e.g., Fig. 3a).

⁴ This is because the distribution of Π is approximately log-normal, which yields a significant tail towards high values when converted to linear space.

If such variations in orientation do make a significant contribution to the observed distribution of bow shock shapes in the Π – Λ plane, then various predictions follow, which might be observationally tested. High-planitude sources with $\Pi > 3$ would be expected to have low inclinations, $|i| < 30^\circ$, whereas high-alatitude sources with $\Lambda > 2$ would be expected to have high inclinations, $|i| > 45^\circ$. Unfortunately, determination of the inclination for individual sources requires high resolution spectroscopy of emission lines in order to map the kinematics of the flow in the bow shock shell (e.g., Henney et al. 2013). This is not currently available for the majority of the MIPS GAL sources, which are detected only by their dust continuum emission. A further prediction for the high-alatitude sources is that the environmental flow should be divergent rather than plane-parallel, in order to give a cantoid shape instead of a wilkinoid. This would tend to favor “weather-vane” cases, where the interstellar medium is flowing past the star, and disfavor “runaway” cases, where the star is moving through a static medium. However, in § 2.4 we found no significant difference in the shape distributions as a function of the bow shock environment. Figure 5a shows that the alitudes of sources that are facing H II regions or 8 μm bright-rimmed clouds (and therefore might be expected to be immersed in a champagne flow) are no higher than sources that are isolated.

5.1.2 Perturbations to the bow shape

An alternative explanation for the variety of observed bow shock shapes is that they are due to time-dependent perturbations to an underlying base shape. For instance, multiple studies have shown that stellar bow shock shells can be unstable (Dgani et al. 1996a,b; Blondin & Koerwer 1998; Comeron & Kaper 1998; Meyer et al. 2014a), leading to large amplitude oscillations in the shell shape. The oscillations are found to be most vigorous when the post shock cooling is highly efficient, allowing the formation of a thin shell (see Paper I). Even in cases where the shell is stable, oscillations may be driven by periodic variations in the stellar wind mass-loss rate or velocity, or by inhomogeneities in the ambient stream. Rather than using a particular dynamical model of these oscillations, we instead crudely simulate their effect by assuming a constant amplitude standing wave perturbation to the base shape, as described in Appendix B. Example results are shown in Figure 13 for an ensemble of bow shocks with different orientations and phases of oscillation, considering three different underlying base shapes. It can be seen that modest amplitudes of 10 to 20% can give rise to a distribution in Π and Λ similar to that observed for the MIPS GAL sources when the oscillation wavelength is of the same order as the bow shock size.

An attractive feature of the oscillation hypothesis is that it naturally explains why we find little correlation between the bow shock shape and other source parameters (§ 2.4), since the instantaneous shape at any instant is largely a matter of chance rather than being due to any intrinsic property of the source. The one significant correlation that we do find is that the alatitude distribution is broader for bow shocks with larger angular sizes. This might be explained if the relative amplitude of oscillations were higher for sources with more powerful winds. Meyer et al. (2016) in their Fig. 2 plot the “axis ratio” (which is our Λ^{-1}) as a function of apex distance for a large set of hydrodynamic bow shock simulations. They find the most unstable bow shocks (with the largest spread in Λ) to be those associated with the highest mass stars in a relatively dense medium, which have apex distances of 0.3 pc to 1 pc. This corresponds to $R_0 > 15''$ for distances less than 4 kpc, which is larger than the median angular

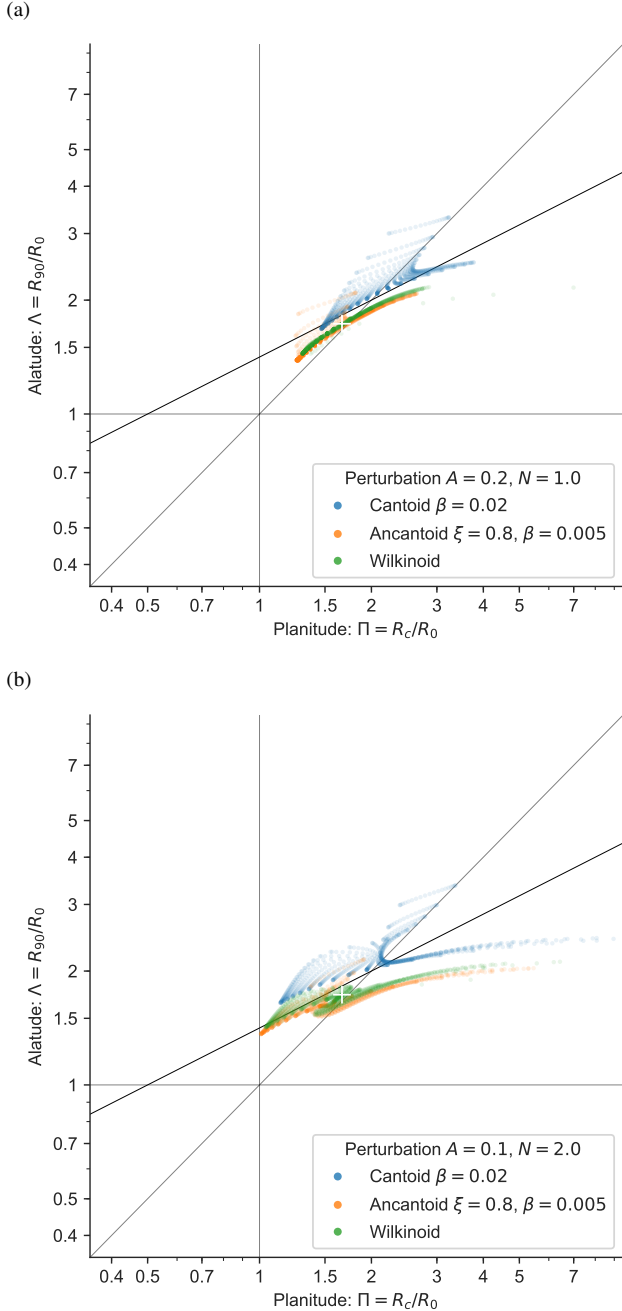


Figure 13. Diagnostic diagram for perturbed shapes from standing wave oscillations. Each model is characterized by a base shape (colored symbols, as described in key) and an amplitude, A , and wavenumber, N , of the oscillation: (a) breathing mode with $N = 1$, $A = 0.2$; (b) curling mode with $N = 2$, $A = 0.1$ (see Fig. B1 for the phase-dependent intrinsic shapes). The plotted points show the varying planitude and alatitude of the projected bow shock shapes with uniform sampling over an entire period of the oscillation and for varying inclinations (sampled according to an isotropic distribution of orientations). Each individual point is plotted with a low opacity so that the crowding of points in certain regions of the plane can be appreciated.

size for the MIPS GAL sources, making this a plausible explanation for our statistical result.

5.2 Variations between different source classes

We now address the difference in shape distribution between the different classes of source. Compared with the OB star bow shocks, the cool star sample from Cox et al. (2012)⁵ shows a significantly smaller alatitude of $\Lambda = 1.41 \pm 0.03$ (see Fig. 10).⁶ Such a closed shape for the wings is inconsistent with the wilkinoid value of $\Lambda = 1.63$ to 1.73 , which is surprising given that the emission shells in these sources are relatively narrow (Figs. 8 and 9), so one might have thought that the thin-shell approximation of Wilkin (1996) would be *more* appropriate than for the OB stars, but this is clearly not the case. One possible explanation for this might be that the bow shocks have not had time to reach a steady-state configuration, as was suggested by Mohamed et al. (2012) for the case of α Ori. The dynamical timescales, R_0/V_w , for the cool star bow shocks are of order 10^4 yr and numerical simulations (e.g., Fig. 11 of Mohamed et al. 2012 and Fig. 2 of van Marle et al. 2014) show that the bow shock wings take of order 3×10^4 yr to 10^5 yr to fully unfold. However, this is still short compared with typical RSG and AGB lifetimes, so while it might apply to a single source it does not work as an explanation for an entire class of sources, especially given that the alatitude and planitude distributions for these sources are so narrow (Fig. 10). A more promising explanation is that the shape difference reflects a different origin for the infrared-emitting dust. In hot stars, the stellar wind is dust-free, so the only dust shell comes from the interstellar medium and lies outside the astropause (contact discontinuity). In cool stars, the stellar wind is also dusty, which could give rise to significant infrared emission from near the stellar wind's termination shock, as has been found from hydrodynamic simulations (Meyer et al. 2014b). This is certainly the case for at least one of our cool star sources, the C-AGB star CW Leo (IRC+10216), where ultraviolet GALEX observations (Sahai & Chronopoulos 2010) clearly show *both* the outer shock and the wind termination shock, and comparison with the Herschel images demonstrate that the infrared dust emission is associated with the latter.

In the case of the Orion Nebula bow shocks (§ 4), we have the opposite situation, where the alatitude and planitude are both significantly larger on average than for the OB star sources (Fig. 12). On the face of it, this is surprising because there are two differences between the source classes that would tend to work in the other direction. First, many of the Orion sources are proplyds, or externally illuminated photoevaporating disks (O'Dell et al. 2008), in which the inner wind is not isotropic but instead is mildly concentrated towards the symmetry axis (García-Arredondo et al. 2001), so that simple models predict an *ancantoid* shape (Tarango-Yong & Henney 2018, § 5) that is less open than for an isotropic wind. Second, as was the case with the cool star sources, both the shocked inner wind and the shocked outer stream are expected to contribute to the emission arcs. Indeed, in several of the sources of Figure 11 (LL 3, 116–3101, 266–558, 308–3036, and LL 5), a two-component emission structure is apparent. In the case of the cool star bow shocks, we invoked this as a possible explanation of their *low* alatitude (see previous

⁵ Three of these sources are high-mass red supergiant (RSG) stars, while the remaining 13 are intermediate-mass asymptotic giant branch (AGB) stars.

⁶ Although the planitude also appears to be slightly smaller, this is not very statistically significant due to the small number of cool star sources and the large width of the OB star planitude distribution.

paragraph), so some stronger countervailing factor is necessary in order to explain why the opposite is seen in the Orion Nebula bow shocks.

Four possible origins for this countervailing factor suggest themselves: (i) the external flow may be more divergent in the Orion sources; (ii) the Mach number of the external flow may be systematically lower; (iii) the fact that the arcs are observed in recombination line emission instead of dust continuum may cause different observational biases; (iv) the shapes may be influenced by collimated jet outflows from the young stars. We now address each of these in turn.

In case (i) one would expect Π and Λ to be positively correlated with R_0/D , where R_0 is the bow shock size (star–apex separation) and D is the distance from the center of divergence of the external flow. In § 4 we found that these are indeed correlated, but only weakly. A more serious objection to this idea is that according to hypersonic thin-shell models (Canto et al. 1996) the momentum ratio parameter β must be relatively large in order to give significantly open bow shock shapes. From Figure 20 of Paper 0 we see that $\beta > 10^{-3}$ is required in order to give $\Pi, \Lambda > 2$. However, for small β one has $\beta \approx (R_0/D)^2$, which yields $\beta = 4 \times 10^{-6}$ to 3×10^{-4} for our sources, so that divergence ought to have little effect on the shapes.

Case (ii) arises from the fact that, if the hypersonic assumption is relaxed, then the opening angle between the outer bow shock and the contact discontinuity in the wings becomes increasingly large as the Mach number, M , drops towards unity. This is a consequence of the *shock polar* relation for oblique shocks (Landau & Lifshitz 1987, §§ 92 and 113) and applies to both the radiative and non-radiative case. It will tend to produce more open shapes, at least in the case that the emission is dominated by the outer shell. At the same time, the relative thickness of the shell, h/R_0 , is predicted to increase as M decreases (e.g., eq [35] of Paper I). We have therefore measured h/R_0 for the Orion sources, finding values ranging from 0.3 to 0.8 with median of 0.5. We have not measured h/R_0 for the full MIPS GAL sample, but Figure 11 of Paper III gives the values for the sub-sample of OB bow shocks studied by (Kobulnicky et al. 2018). The median value is 0.2, implying thinner shells than in the Orion Nebula bow shocks, which lends support to the idea that the Mach number may be lower in the latter. However, among the Orion sources we find that h/R_0 is completely uncorrelated with either Π or Λ ($r = 0.02$ and -0.05 , respectively).

Case (iii) attempts to explain the difference in shapes as a result of an “optical illusion” whereby the OB star bow shocks are in reality more open than they appear. The hydrogen recombination line surface brightness from an isothermal shell is proportional to the emission measure (line of sight integral of the product of proton and electron densities), whereas the mid-infrared surface brightness is not simply proportional to the dust column density, since it results from the reprocessing of stellar radiation. For typical bow shock grain temperatures ($T = 50$ to 100 K, Kobulnicky et al. 2017) the $24\ \mu\text{m}$ band used for the OB star sample lies on the short wavelength Wien side of the dust emission spectrum, which gives a very steep radial dependence of the emissivity. Acreman et al. (2016) calculate synthetic emission maps from hydrodynamical simulations and show that, even for a relatively thin bow shock shell, the emission arc seen in $H\alpha$ tends to be more open than the arc seen in the mid-infrared (see their Fig. 3). The effect should be even larger for thicker shells, as demonstrated by Mackey et al. (2016), who simulate the subsonic motion of an O star through its $H\text{II}$ region and show that this can give rise to an *apparent* bow shock at $24\ \mu\text{m}$ even when there is no corresponding dense shell at all.

Finally, case (iv) arises from the observation that several of the Orion sources possess high velocity ($> 100\ \text{km s}^{-1}$) collimated jets (Bally et al. 2006), which produce strings of emission knots that partially overlap the wings of the bow shock. In the case of 109–246, LL 1, LL 4, LL 5, and LL 6, the projected jet axis is roughly perpendicular to the projected bow shock axis, and two of these (109–246 and LL 6) have the most extreme high values of Π and Λ . There are several other Orion Nebula bow shock sources with perpendicular jets (LL 2, 203–3039, 261–3018, 344–3020, and LL 7), which we omitted from our sample because of difficulty in measuring Λ , but the majority also have large planitudes $\Pi > 5$. Only one source, 4468–605, has a jet oriented parallel to the bow shock axis, and this has the smallest Π and third-smallest Λ of the sample. The circumstantial evidence thus points towards the jets playing some role in shaping the bow shocks when they are oriented perpendicular to the axis, even though we took care when tracing the bow shock ridges to avoid any region with superimposed jet knots. This would break the cylindrical symmetry of the bow shock, which should have a kinematic signature. However, in the only two sources that have been studied kinematically (Henney et al. 2013), the bow shock shell does not show any sign of the red/blue asymmetry that is seen in the jet knots, which argues against any such association.

6 SUMMARY

We have presented a statistical study of the shapes of three different classes of stellar bow shocks, as characterized by their flatness of apex (planitude, Π) and openness of wings (alatude, Λ), following the terminology of Tarango-Yong & Henney (2018, Paper 0). Our principal findings are as follows:

1. Bow shocks driven by hot OB stars, from the mid-infrared catalog of Kobulnicky et al. (2016), have an average shape $(\Pi, \Lambda) \approx (1.6, 1.7)$ that is consistent with predictions of the Wilkin (1996) analytic model, but the dispersion in observed shapes $(\sigma_\Pi, \sigma_\Lambda) \approx (0.9, 0.3)$ is many times larger than predicted by that model.
2. The bow shock shapes show little correlation with other parameters of the source, such as stellar magnitude, Galactic latitude or longitude, extinction, or type of environment (cluster versus isolated). The only exception is that the dispersion in alatude is higher for bow shocks of larger angular size.
3. A possible explanation for the previous results is that the variation in shapes is caused by time dependent oscillations in the bow shock surface, with relative amplitude of 10 to 20% and wavelength of order the bow shock size. The oscillations may either be due to dynamic instabilities in the bow shock shell or be driven by temporal variations in the stellar wind. If the oscillations were more vigorous for stars with more powerful winds, it could explain the correlation with angular size.
4. Bow shocks driven by cool luminous stars (red supergiants and asymptotic giant branch stars), from the catalog of (Cox et al. 2012), have an average shape $(\Pi, \Lambda) \approx (1.5, 1.4)$, which has a significantly smaller alatude than the OB star sources, and which is not consistent with the Wilkin (1996) model. We suggest that this may be due to their dust emission being dominated by shocked stellar wind material, instead of shocked ambient material as is the case with the OB stars.
5. Bow shocks driven by proplyds and other young stars in the outer regions of the Orion Nebula, from the catalogs of Bally et al. (2006) and Gutiérrez-Soto (2015), have an average shape of $(\Pi, \Lambda) \approx (2.7, 2.4)$, with a significant tail up to $(\Pi, \Lambda) \approx (7, 4)$.

A minority of these sources ($\approx 20\%$) have shapes similar to the OB star bow shocks, but the remainder have much flatter apexes and more open wings. We suggest several possible mechanisms to explain this difference: divergent ambient flow; low Mach number; observational biases; influence of collimated jets, but the available evidence for and against each of these is mixed.

ACKNOWLEDGEMENTS

We are grateful for financial support provided by Dirección General de Asuntos del Personal Académico, Universidad Nacional Autónoma de México, through grants Programa de Apoyo a Proyectos de Investigación e Innovación Tecnológica IN111215 and IN107019.

REFERENCES

- Acreman D. M., Stevens I. R., Harries T. J., 2016, *MNRAS*, 456, 136
- Anderson T. W., Darling D. A., 1952, *Ann. Math. Statist.*, 23, 193
- Arthur S. J., Hoare M. G., 2006, *ApJS*, 165, 283
- Astropy Collaboration et al., 2018, *AJ*, 156, 123
- Bally J., Reipurth B., 2001, *ApJ*, 546, 299
- Bally J., Sutherland R. S., Devine D., Johnstone D., 1998, *AJ*, 116, 293
- Bally J., O'Dell C. R., McCaughrean M. J., 2000, *AJ*, 119, 2919
- Bally J., Licht D., Smith N., Walawender J., 2006, *AJ*, 131, 473
- Baranov V. B., Krasnobaev K. V., Kulikovskii A. G., 1970, *Akademiia Nauk SSSR Doklady*, 194, 41
- Baranov V. B., Krasnobaev K. V., Kulikovskii A. G., 1971, *Soviet Physics Doklady*, 15, 791
- Benaglia P., Romero G. E., Martí J., Peri C. S., Araudo A. T., 2010, *A&A*, 517, L10
- Blondin J. M., Koerwer J. F., 1998, *New Astron.*, 3, 571
- Bodensteiner J., Baade D., Greiner J., Langer N., 2018, *A&A*, 618, A110
- Brown D., Bomans D. J., 2005, *A&A*, 439, 183
- Brown M. B., Forsythe A. B., 1974, *Journal of the American Statistical Association*, 69, 364
- Brownsberger S., Romani R. W., 2014, *ApJ*, 784, 154
- Canto J., Raga A. C., Wilkin F. P., 1996, *ApJ*, 469, 729
- Carey S. J., et al., 2009, *PASP*, 121, 76
- Comeron F., Kaper L., 1998, *A&A*, 338, 273
- Cox N. L. J., et al., 2012, *A&A*, 537, A35
- Cureton E. E., 1956, *Psychometrika*, 21, 287
- Cyganowski C. J., Reid M. J., Fish V. L., Ho P. T. P., 2003, *ApJ*, 596, 344
- Dgani R., van Buren D., Noriega-Crespo A., 1996a, *ApJ*, 461, 372
- Dgani R., van Buren D., Noriega-Crespo A., 1996b, *ApJ*, 461, 927
- Dyson J. E., de Vries J., 1972, *A&A*, 20, 223
- Dzib S. A., et al., 2017, *ApJ*, 834, 139
- Eker Z., et al., 2015, *AJ*, 149, 131
- García-Arredondo F., Henney W. J., Arthur S. J., 2001, *ApJ*, 561, 830
- Geballe T. R., Rigaut F., Roy J.-R., Draine B. T., 2004, *ApJ*, 602, 770
- Groenewegen M. A. T., et al., 2011, *A&A*, 526, A162
- Gull T. R., Sofia S., 1979, *ApJ*, 230, 782
- Gutiérrez-Soto L. Á., 2015, Master's thesis, Universidad Nacional Autónoma de México
- Gvaramadze V. V., Bomans D. J., 2008, *A&A*, 490, 1071
- Hayward T. L., Houck J. R., Miles J. W., 1994, *ApJ*, 433, 157
- Head M. L., Holman L., Lanfear R., Kahn A. T., Jennions M. D., 2015, *PLOS Biology*, 13, 1
- Henney W. J., Arthur S. J., 2019a, *MNRAS*, 486, 3423 (Paper I)
- Henney W. J., Arthur S. J., 2019b, *MNRAS*, 486, 4423 (Paper II)
- Henney W. J., Arthur S. J., 2019c, arXiv e-prints, 1904.00343 *MNRAS submitted* (Paper III)
- Henney W. J., Arthur S. J., García-Díaz M. T., 2005, *ApJ*, 627, 813
- Henney W. J., García-Díaz M. T., O'Dell C. R., Rubin R. H., 2013, *MNRAS*, 428, 691
- Immer K., Cyganowski C., Reid M. J., Menten K. M., 2014, *A&A*, 563, A39
- Indebetouw R., et al., 2005, *ApJ*, 619, 931
- Johnstone D., Hollenbach D., Bally J., 1998, *ApJ*, 499, 758
- Joye W. A., Mandel E., 2003, in Payne H. E., Jedrzejewski R. I., Hook R. N., eds, *Astronomical Society of the Pacific Conference Series Vol. 295, Astronomical Data Analysis Software and Systems XII*. p. 489
- Kim D., Lu J. R., Konopacky Q., Chu L., Toller E., Anderson J., Theissen C. A., Morris M. R., 2018, arXiv e-prints
- Klaassen P. D., et al., 2018, *A&A*, 611, A99
- Kobulnicky H. A., Gilbert I. J., Kiminki D. C., 2010, *ApJ*, 710, 549
- Kobulnicky H. A., et al., 2016, *ApJS*, 227, 18
- Kobulnicky H. A., Schurhammer D. P., Baldwin D. J., Chick W. T., Dixon D. M., Lee D., Povich M. S., 2017, *AJ*, 154, 201
- Kobulnicky H. A., Chick W. T., Povich M. S., 2018, *ApJ*, 856, 74 (K18)
- Kulkarni S. R., Hester J. J., 1988, *Nature*, 335, 801
- Landau L. D., Lifshitz E. M., 1987, *Fluid Mechanics, Second Edition: Volume 6 (Course of Theoretical Physics)*, 2 edn. Course of theoretical physics / by L. D. Landau and E. M. Lifshitz, Vol. 6, Butterworth-Heinemann
- Leiva-Murillo J. M., Artés-Rodríguez A., 2012, *Pattern Recogn. Lett.*, 33, 1717
- Mac Low M.-M., van Buren D., Wood D. O. S., Churchwell E., 1991, *ApJ*, 369, 395
- Mackey J., Gvaramadze V. V., Mohamed S., Langer N., 2015, *A&A*, 573, A10
- Mackey J., Haworth T. J., Gvaramadze V. V., Mohamed S., Langer N., Harries T. J., 2016, *A&A*, 586, A114
- Majewski S. R., Zasowski G., Nidever D. L., 2011, *ApJ*, 739, 25
- Makarov A. A., Simonova G. I., 2017, *Journal of Mathematical Sciences*, 221, 580
- Mann H. B., Whitney D. R., 1947, *The Annals of Mathematical Statistics*, 18, 50
- Meyer D. M.-A., Gvaramadze V. V., Langer N., Mackey J., Boumis P., Mohamed S., 2014a, *MNRAS*, 439, L41
- Meyer D. M.-A., Mackey J., Langer N., Gvaramadze V. V., Mignone A., Izzard R. G., Kaper L., 2014b, *MNRAS*, 444, 2754
- Meyer D. M.-A., van Marle A.-J., Kuiper R., Kley W., 2016, *MNRAS*, 459, 1146
- Meyer D. M.-A., Mignone A., Kuiper R., Raga A. C., Kley W., 2017, *MNRAS*, 464, 3229
- Mohamed S., Mackey J., Langer N., 2012, *A&A*, 541, A1
- Noriega-Crespo A., van Buren D., Dgani R., 1997, *AJ*, 113, 780
- O'Dell C. R., 2001, *AJ*, 122, 2662
- O'Dell C. R., Wen Z., 1994, *ApJ*, 436, 194
- O'Dell C. R., Wen Z., Hu X., 1993, *ApJ*, 410, 696
- O'Dell C. R., Muench A., Smith N., Zapata L., 2008, *Star Formation in the Orion Nebula II: Gas, Dust, Proplyds and Outflows*. p. 544
- Paltani S., 2004, *A&A*, 420, 789
- Peri C. S., Benaglia P., Brookes D. P., Stevens I. R., Isequilla N. L., 2012, *A&A*, 538, A108
- Peri C. S., Benaglia P., Isequilla N. L., 2015, *A&A*, 578, A45
- Pikel'ner S. B., 1968, *Astrophys. Lett.*, 2, 97
- Povich M. S., Benjamin R. A., Whitney B. A., Babler B. L., Indebetouw R., Meade M. R., Churchwell E., 2008, *ApJ*, 689, 242
- Puls J., et al., 1996, *A&A*, 305, 171
- Reid M. J., Ho P. T. P., 1985, *ApJ*, 288, L17
- Robberto M., et al., 2005, *AJ*, 129, 1534
- Robberto M., et al., 2013, *ApJS*, 207, 10
- Sahai R., Chronopoulos C. K., 2010, *ApJ*, 711, L53
- Sahai R., Güsten R., Morris M. R., 2012, *ApJ*, 761, L21
- Sanchez-Bermudez J., Schödel R., Alberdi A., Muzić K., Hummel C. A., Pott J.-U., 2014, *A&A*, 567, A21
- Scholz F. W., Stephens M. A., 1987, *Journal of the American Statistical Association*, 82, 918
- Scott D. W., 2015, *Multivariate density estimation: theory, practice, and visualization*, 2nd edn. John Wiley & Sons
- Sexton R. O., Povich M. S., Smith N., Babler B. L., Meade M. R., Rudolph A. L., 2015, *MNRAS*, 446, 1047
- Smith N., Bally J., Shuping R. Y., Morris M., Kassiss M., 2005, *AJ*, 130, 1763
- Steggles H. G., Hoare M. G., Pittard J. M., 2017, *MNRAS*, 466, 4573

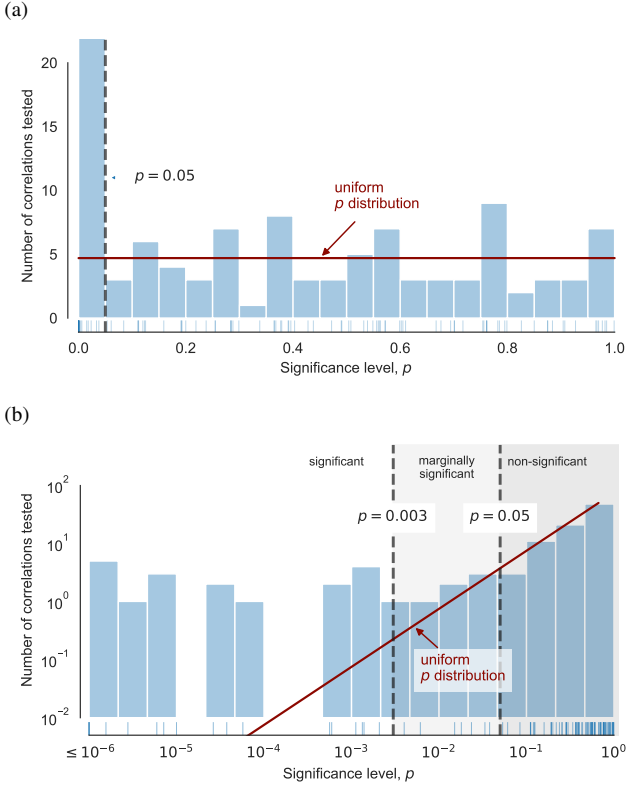


Figure A1. Histogram of p -values for all non-parametric 2-sample tests listed in Table A1. (a) Uniformly spaced linear bins and linear vertical axis. (b) Uniformly spaced logarithmic bins and logarithmic vertical axis, with all values $p \leq 10^{-6}$ included in the leftmost bin. Short thin vertical lines above the horizontal axis show the individual values. The thick vertical dashed lines show the traditional threshold values for significance: $p = 0.003$ ($\approx 3\sigma$) and $p = 0.05$ ($\approx 2\sigma$). The red solid line shows the uniform distribution of p -values that would be expected if the null hypothesis were always true, that is, if no significant correlations existed.

- Stephens M. A., 1970, *Journal of the Royal Statistical Society. Series B (Methodological)*, 32, 115
 Tanner A., Ghez A. M., Morris M. R., Christou J. C., 2005, *ApJ*, 624, 742
 Tarango-Yong J. A., Henney W. J., 2018, *MNRAS*, 477, 2431 (Paper 0)
 Ueta T., et al., 2006, *ApJ*, 648, L39
 Ueta T., et al., 2008, *PASJ*, 60, S407
 Weilbacher P. M., et al., 2015, *A&A*, 582, A114
 Werner M. W., et al., 2004, *ApJS*, 154, 1
 Wilkin F. P., 1996, *ApJ*, 459, L31
 Wood D. O. S., Churchwell E., 1989, *ApJS*, 69, 831
 Wright E. L., et al., 2010, *AJ*, 140, 1868
 Zuckerman B., 1973, *ApJ*, 183, 863
 van Buren D., McCray R., 1988, *ApJ*, 329, L93
 van Buren D., Mac Low M.-M., Wood D. O. S., Churchwell E., 1990, *ApJ*, 353, 570
 van Buren D., Noriega-Crespo A., Dgani R., 1995, *AJ*, 110, 2914
 van Marle A. J., Decin L., Meliani Z., 2014, *A&A*, 561, A152

APPENDIX A: DISTRIBUTION OF P-VALUES FOR ALL CORRELATIONS TESTED

Results from all the statistical tests of the shape distributions discussed in § 2.4 are given in Table A1. The p -values are the probability of finding a difference between two populations at least as large as

what is observed *given* that there is no difference in the underlying distribution from which the two populations are drawn (that is, given that the null hypothesis is true). Conventionally, the null hypothesis is rejected at a certain significance threshold α when $p < \alpha$. Since we are blindly testing many different hypotheses at once, the commonly used $\alpha = 0.05$ threshold is too lenient. In Figure A1 we analyse the frequency distribution of p from all our tests (see Head et al. 2015), finding a systematic excess over a uniform distribution only for $p < 0.01$. We therefore take $\alpha = 0.003$ as the optimum threshold in order to balance the risks of false positives and false negatives. A false positive is the erroneous rejection of the null hypothesis (the spurious detection of a correlation that is not really there), while a false negative is failing to detect a true correlation.

APPENDIX B: PERTURBED BOW SHOCKS

In this appendix, we present a highly idealized model for small, time-varying perturbations to a steady-state bow shock shape, such as those discussed in § 5 of Paper 0. These perturbations may be due to periodic variations in the momentum-loss rate of one of the winds, or due to dynamical instabilities in the shocked shell.

We consider fractional perturbations $\Delta(\theta, t)$ of a base shape $R(\theta)$, such that $R(\theta) \rightarrow [1 + \Delta(\theta, t)]R(\theta)$. For simplicity, $\Delta(\theta, t)$ is a standing wave of constant amplitude A , which is periodic in θ , with wave number N . We assume that the oscillation occurs simultaneously and coherently at all azimuths, so that cylindrical symmetry is maintained. This implies that $\Delta(\theta, t)$ must be even in θ , so can be expressed as

$$\Delta(\theta, t) = A \cos(N\theta) \cos(2\pi\varphi). \quad (\text{B1})$$

For waves with period P , the fractional phase φ will vary with time t as

$$\varphi(t) = (\varphi_0 + t/P) \bmod 1.0, \quad (\text{B2})$$

where φ_0 is an arbitrary reference phase.

Example oscillations with wave numbers $N = 1.0, 2.0$, and 5.0 superimposed on a wilkinoid base shape are shown in Figure B1. There are N nodes of the oscillation between $\theta = [0, \pi]$, always with an antinode at the apex ($\theta = 0$), as required by symmetry. So, with $N = 1.0$ there is a node (fixed point) in the near wing at $\theta = \pi/2$, but an antinode in the far wing at $\theta = \pi$, which is in antiphase with the oscillation of the apex, giving rise to a large-scale “breathing” mode of oscillation. With $N = 2.0$, there are nodes at $\theta = \pi/4$ and $3\pi/4$, while the antiphase antinode has moved to the near wing at $\theta = \pi/2$. There is still an antinode in the far wing at $\theta = \pi$ but it is now in phase with the apex, giving rise to a “curling-up/straightening-out” mode of oscillation. With $N = 5.0$, there are many more nodes and antinodes, giving a “ringing” mode of oscillation. Note that all our examples have $A \propto 1/N$ in order to keep the local curvature relatively low. If the product AN is not small compared to unity, then the local curvature can be so extreme as to reverse the concave shape of the base bow shape, producing locally convex regions.

If the bow shape is viewed at different inclinations, then the effect of the oscillations on the projected shape will vary. In particular, the apex-to-wing interval in body-frame angle changes from $\theta = [0, \pi/2]$ at $i = 0$ to $\theta = [\theta_0, \theta_{90}]$ for general i , see equations (18) and (21) of Paper 0. The difference $\theta_{90} - \theta_0$ is always a decreasing function of $|i|$, so the oscillations of the tangent line become increasingly stretched out as the inclination increases. This effect can be seen in Figure B2, which shows an example of the variation in projected perturbed shape with inclination angle for 3 different phases, this

Table A1. Results of all statistical tests performed on observed bow shock shape parameters. Significant correlations are shown in **bold**, marginally significant correlations in *italic*

Comparison (1)	Dependent Variable (2)	Mean		Std. Dev.		Obs. Disp.		Effect sizes			Non-parametric test <i>p</i> -values		
		$\langle A \rangle$	$\langle B \rangle$	σ_A	σ_B	$\langle \epsilon_A \rangle$	$\langle \epsilon_B \rangle$	r_b	Cohen <i>d</i>	σ_A/σ_B	K-S	Rank	B-F
		(3)	(4)	(5)	(6)	(7)	(8)	(9)	(10)	(11)	(12)	(13)	(14)
<i>Median split of continuous independent variables</i>													
Faint/bright	Π	1.66	1.92	0.63	1.05	0.097	0.078	0.12	0.30	<i>1.65</i>	0.57	0.11	<i>0.034</i>
<i>H</i> magnitude	Λ	1.68	1.77	0.27	0.32	0.23	0.24	<i>0.17</i>	<i>0.31</i>	1.18	<i>0.018</i>	<i>0.024</i>	0.13
$n_A = n_B = 113$	$\Delta\Lambda$	0.18	0.20	0.16	0.16			0.070	0.093	1.01	0.47	0.37	0.76
Low/high	Π	1.77	1.80	0.98	0.76	0.11	0.062	0.10	0.043	0.77	0.51	0.19	0.60
bow shock size, R_0	Λ	1.71	1.74	0.25	0.34	0.26	0.21	0.061	0.11	1.34	0.0021	0.43	0.0014
$n_A = n_B = 113$	$\Delta\Lambda$	0.18	0.20	0.16	0.17			0.091	0.18	1.05	<i>0.0061</i>	0.24	0.19
Low/high	Π	1.73	1.85	0.82	0.92	0.091	0.085	0.082	0.14	1.12	0.38	0.29	0.98
extinction, A_K	Λ	1.70	1.74	0.27	0.32	0.23	0.24	0.040	0.13	1.21	0.57	0.60	0.12
$n_A = n_B = 113$	$\Delta\Lambda$	0.19	0.20	0.14	0.18			-0.039	0.057	1.33	0.061	0.61	0.11
Low/high	Π	1.71	1.86	0.73	0.99	0.085	0.091	0.069	0.18	1.36	<i>0.038</i>	0.37	0.084
$ b $	Λ	1.72	1.72	0.33	0.26	0.23	0.23	0.020	0.0080	0.80	0.26	0.80	0.053
$n_A = n_B = 113$	$\Delta\Lambda$	0.19	0.19	0.16	0.16			0.0090	0.021	1.01	0.88	0.91	0.69
High/low	Π	1.81	1.75	0.95	0.74	0.090	0.084	0.	-0.064	0.79	0.99	1.00	0.55
$\cos \ell$	Λ	1.73	1.71	0.28	0.32	0.24	0.22	-0.049	-0.093	1.15	0.50	0.53	0.16
$n_A, n_B = 137, 90$	$\Delta\Lambda$	0.18	0.20	0.16	0.17			0.054	0.12	1.10	0.76	0.49	0.37
<i>Categorical independent variables</i>													
Environment:	Π	1.76	1.85	0.85	0.90	0.087	0.083	0.042	0.11	1.05	0.72	0.68	0.38
Isolated vs Facing	Λ	1.74	1.69	0.28	0.34	0.24	0.22	-0.070	-0.14	1.19	0.97	0.49	0.39
$n_A, n_B = 170, 41$	$\Delta\Lambda$	0.19	0.20	0.16	0.17			-0.019	0.034	1.07	0.56	0.85	0.44
Environment:	Π	1.76	1.91	0.85	0.96	0.087	0.11	0.024	0.17	1.12	0.28	0.88	0.26
Isolated vs H II	Λ	1.74	1.68	0.28	0.31	0.24	0.23	-0.13	-0.19	1.09	0.70	0.39	0.78
$n_A, n_B = 170, 16$	$\Delta\Lambda$	0.19	0.18	0.16	0.14			-0.048	-0.095	0.86	0.79	0.75	0.80
Single/multiple	Π	1.77	1.83	0.83	0.99	0.090	0.080	0.027	0.076	1.20	0.98	0.76	0.61
source candidate	Λ	1.71	1.76	0.29	0.32	0.23	0.24	0.074	0.18	1.09	0.11	0.40	0.34
$n_A, n_B = 167, 60$	$\Delta\Lambda$	0.18	0.21	0.16	0.16			0.093	0.14	0.99	0.56	0.28	0.97
With/without	Π	1.71	1.80	0.60	0.93	0.091	0.087	-0.012	0.10	1.55	0.88	0.90	0.20
8 μ m emission	Λ	1.73	1.72	0.29	0.30	0.22	0.24	-0.042	-0.044	1.03	0.30	0.67	0.56
$n_A, n_B = 45, 182$	$\Delta\Lambda$	0.20	0.19	0.21	0.15			0.021	-0.11	0.73	0.97	0.83	0.22
3-star vs (4+5)-star	Π	1.63	2.00	0.91	0.76	0.11	0.061	0.39	0.43	0.84	3.8×10^{-5}	7.7×10^{-7}	0.76
	Λ	1.66	1.81	0.29	0.29	0.25	0.22	0.33	0.53	0.99	0.000 56	2.6×10^{-5}	0.40
$n_A, n_B = 133, 94$	$\Delta\Lambda$	0.19	0.19	0.16	0.16			-0.0070	0.0090	0.99	0.54	0.93	0.56
<i>Intercomparison with other datasets</i>													
MIPS vs Orion	Π	1.78	3.09	0.87	1.67			0.57	1.4	1.91	0.0011	5.7×10^{-5}	0.0013
	Λ	1.72	2.53	0.30	0.75			0.71	2.3	2.53	10.0×10^{-6}	5.5×10^{-7}	1.5×10^{-9}
$n_A, n_B = 227, 18$	$\Delta\Lambda$	0.19	0.66	0.16	0.51			0.64	2.2	3.17	7.1×10^{-6}	6.0×10^{-6}	1.1×10^{-10}
MIPS vs RSG	Π	1.78	1.48	0.87	0.23			-0.16	-0.36	<i>0.26</i>	0.000 59	0.29	<i>0.015</i>
	Λ	1.72	1.41	0.30	0.10			-0.72	-1.1	<i>0.34</i>	2.8×10^{-6}	1.6×10^{-6}	<i>0.0040</i>
$n_A, n_B = 227, 16$	$\Delta\Lambda$	0.19	0.15	0.16	0.08			-0.072	-0.27	0.47	0.19	0.70	0.12

Description of columns: (Col. 1) How the two A/B source sub-samples are defined, also giving the size of each sub-sample, n_A and n_B . (Col. 2) Dependent variable whose distribution is compared between the two sub-samples. (Cols. 3–6) Mean and standard deviation, σ , of the dependent variable for each of the two sub-samples. (Cols. 7–8) Mean over each sub-sample of the observational dispersion (ϵ , standard deviation) of radii that contribute to the dependent variable for each individual source, as in steps 6 and 8 of § 2.1. Note that in the case of Π , this is $\epsilon(R_0)$, and so is not a direct measure of the observational uncertainty in Π . (Cols. 9–11) Standardized “effect sizes”, which are dimensionless measures of the difference in the distribution of the dependent variable between the two sub-samples. (Col. 9) Rank biserial correlation coefficient (Cureton 1956), which is obtained by considering all $n_A n_B$ pair-wise comparisons of the dependent variable between a source in sub-sample A and a source in sub-sample B. It is the difference between the fraction of such comparisons “won” by sub-sample A and those “won” by sub-sample B, and thus may vary between -1 and +1. (Col. 10) Cohen’s *d*, which is a dimensionless mean difference: $d = (\langle A \rangle - \langle B \rangle) / \sigma_{\text{pool}}$, where $\sigma_{\text{pool}} = (n_A \sigma_A^2 + n_B \sigma_B^2)^{1/2} / \sqrt{n_A + n_B}$ is the pooled standard deviation. (Col. 11) Ratio of standard deviations between the two sub-samples. (Cols. 12–14) Probabilities (*p*-values) of the two sub-samples being as different as observed if they were to be drawn from the same population, according to three different non-parametric tests. (Col. 12) Kuiper 2-sample test, which is a general test of similarity between two distributions that is designed to retain sensitivity to differences in the tails of the distributions. (Col. 13) Mann–Whitney–Wilcoxon *U* test (Mann & Whitney 1947), which is sensitive to differences in the central value of the distributions. (Col. 14) Brown–Forsythe test for equality of variance (Brown & Forsythe 1974)

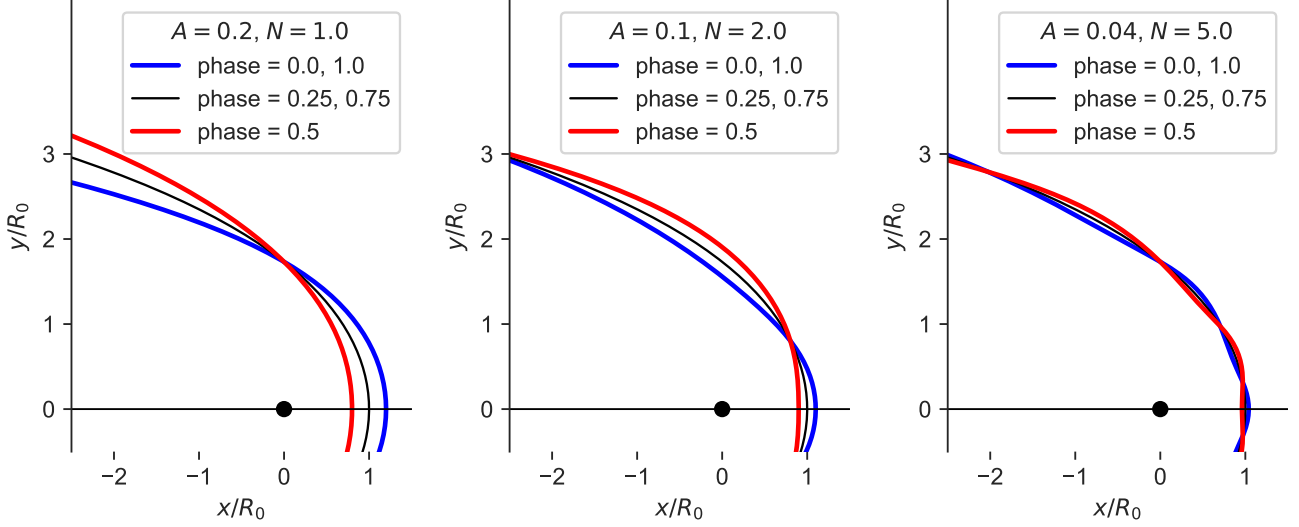


Figure B1. Small-amplitude standing wave perturbations to wilkinoid bow shapes. The maximum deviations from the base shape are seen at phases $\phi = 0$ (blue line) and $\phi = 0.5$ (red line), while the perturbation is zero at $\phi = 0.25$ and 0.75 (black line). Results are shown left to right for increasing wave numbers N and decreasing amplitudes A : (a) $A = 0.2$, $N = 1.0$, (b) $A = 0.1$, $N = 2.0$, (c) $A = 0.04$, $N = 5.0$. The maximum curvature, proportional to AN is the same in all three cases.

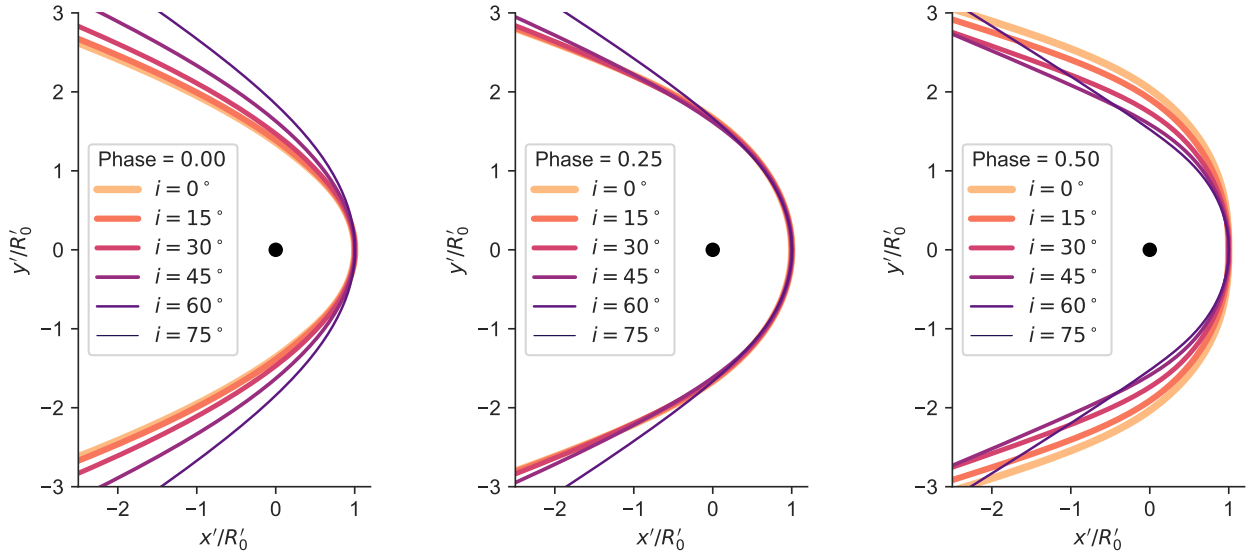


Figure B2. Plane-of-sky projections of perturbed bow shapes. In all cases, the base bow shape is ancantoid with $\xi = 0.8$, $\beta = 0.005$ and the perturbation is the curling mode shown in the central panel of Fig. B1, with amplitude $A = 0.1$ and wave number $N = 2.0$. Results are shown for inclination angles $i = 0$ to $i = 75^\circ$ (indicated by line color and thickness, see key) and for different fractional phases of the oscillation: (a) $\phi = 0.0$, (b) $\phi = 0.25$, (c) $\phi = 0.50$. Unlike in Fig. B1, the spatial coordinates are normalized to the instantaneous projected apex radius R'_0 at each phase, so the apex does not appear to move.

time for an ancantoid base shape and the $N = 2.0$ perturbation shown in Figure B1b. The most marked changes with phase are seen for low inclinations (light colored lines), whereas the changes are smaller, although still noticeable, for $|i| \geq 45^\circ$. If AN exceeds about 0.5, then the local curvature of the perturbations is so extreme that multiple tangent lines exist at intermediate inclinations, which produces the appearance of additional incomplete bright arcs inside the main arc of the bow.

This paper has been typeset from a \LaTeX file prepared by the author.